Geochemistry of the Early Cretaceous saline lacustrine shales on the Lingshan Island, East China: implications for provenance, tectonic setting, and paleoweathering

Xiangyu Zhang[1,2], Lu Liu[1], Qiang Sun[3], Yanming Xu[4], Shoujun Li[5], Xiaoli Wang[1], Xuxue Wang[5], Ying Sun[1], and Wenxia Wang[1,6]*

[1]College of life Sciences, Linyi University, Linyi, Shandong 276000, China
[2]Key Laboratory of Stratigraphy and Paleontology, Ministry of Natural Resources, Beijing 100037, China
[3]Shandong GREHEE Group Co. LTD., Jinan, Shandong 250100, China
[4]No.7 Exploration Institute of Geology and Mineral Resources, Linyi, Shandong 276006, China
[5]College of Earth Science & Engineering, Shandong University of Science and Technology, Qingdao, Shandong 266590, China
[6]State Key Laboratory of Lake Science and Environment, Nanjing Institute of Geography and Limnology, Chinese Academy of Sciences, Nanjing 210008, China

ABSTRACT: Early Cretaceous saline lacustrine black shales in the Fajiaying Formation were deposited under hothouse conditions and have a complex structure and history of sedimentary evolution. In this study, integrated petrographic and geochemical investigations were utilized to determine the provenance, tectonic setting, and paleoweathering conditions of these shales, therefore revealing their depositional history. Shale in the area under investigation has not been subjected to any post-depositional alteration, mechanical sorting, or recycling, hence its geochemistry has not been affected. The chondrite normalized rare earth elements (REE) pattern of shales displayed typical characteristics, including an enrichment in light REE (LREE), a flat pattern for heavy REE (HREE), and a negative europium (Eu) anomaly. Specific trace element ratios suggested that the sediments were primarily derived from felsic source rocks. Furthermore, there was no discernible shift in the sediment source between the Qiancengya and the Laohuzui sections. The discrimination diagrams of major and trace elements used to understand the tectonic history showed that the majority of the source rocks originated from the active continental margin (ACM) and continental island-arc (CIArc). The bivariate plots and low average values of CIW (chemical index of weathering) and CIA (chemical index of alteration) for the examined shale suggested that chemical weathering in the source terrain under arid conditions was extremely weak. Importantly, with the change of climate from dry-hot to warm-humid, an increase in CIA and CIW was observed which indicated a gradual increase in chemical weathering.

Key words: Early Cretaceous, Fajiaying Formation, black shales, geochemistry, provenance, tectonic setting, paleoweathering conditions

1. INTRODUCTION

The Cretaceous (145–66 Ma) period in Earth's geological history is known as the greenhouse period (e.g., Wilson et al., 2002; Moriya, 2011; Huber et al., 2018). During this time, several major global geological events occurred, including the formation of major igneous provinces (Tejada et al., 2009; Bottini et al., 2012), oceanic anoxic events (Charbonnier et al., 2018; Fernández-Mendiola et al., 2018), biomass evolution (Heimhofer et al., 2005; Horikx et al., 2017), and cluster extinction (e.g., Erba, 1994). Consequently, the Cretaceous Period has become a research hotspot for academics all over the world.

In recent years, the research on Cretaceous geological events based on continental sedimentary records of East Asia has gradually increased (Zhang and Li, 2020; Zhang et al., 2020a, 2021a, 2021b; Chen et al., 2021; Fan et al., 2021; Nakagawa et al.,

2022; Wheeler et al., 2022; Zhang et al., 2022; Wang, X.X. et al., 2022; Wu et al., 2023). The studies of continental records in China showed that the disappearance of the East China Plateau has resulted in the Cretaceous climate in East China have distinct regional characteristics (Zhang et al., 2008). The arid or semi-arid climate increased evaporation, resulting in the Early Cretaceous water area in the northwest and southeast China being dominated by closed saline lakes, marshes, and ponds in the Early Cretaceous (Li et al., 2013). Geochemical indicators and paleontological data sets of shale from the Lower Cretaceous Laiyang Group in Lingshan Island and Jiaolai Basin of East China indicated that East China belonged to a tropical subtropical climate region during the Early Cretaceous when strong evaporation led to the evolution of some rift lake basins in East China into saline lake basins (Zhang and Li, 2020; Zhang et al., 2020b, 2020c). The Early Cretaceous continental salt lake sediments in China experienced a complex sedimentary process, making it difficult to understand their sedimentary history (Zhong, 2012; Yang et al., 2017; Fan et al., 2020; Zhang et al., 2020c; Ma et al., 2021). The composition of sedimentary rocks plays a significant important role in interpreting general geology (e.g., tectonic setting, provenance, and paleoweathering conditions) because various provenance regions have been destroyed and only the sediments derived from them remain as evidence. The major and trace element contents and relative functions of discrimination of these sediments and characteristic ratios can be used to analyze the source area, suggesting their paleoweathering conditions and sedimentary history (e.g., Madhavaraju et al., 2017; Absar, 2021; Madhavaraju et al., 2021; Ramirez-Montoya et al., 2021). For this study, we collected shales from the Fajiaying Formation that were deposited in a saline lake during the Early Cretaceous greenhouse climate and present the comprehensive and systematic geochemical data (such as trace, major oxides, and rare earth elements; REE) for source rocks characteristics and deciphering paleoweathering conditions. The chemostratigraphic concept has also been applied to the discussion of vertical variations of geochemical proxies, which yield crucial insights into the varying paleoweathering conditions prevailing during the Fajiaying Formation deposition. The current comprehensive study may enhance the knowledge of the evolution of the sedimentary sequences deposited during the Early Cretaceous periods in East China.

2. GEOLOGICAL SETTING

Lingshan Island can be found in the Sulu orogenic belt's oblique eastern margin, which is the collision suture zone between the South China and the North China Plates (Wang et al., 2014; Fig. 1a). It is surrounded by the Qingdao-Wulian Fault Zone to the west and the Qianliyan uplift to the east (after Wang et al., 2014), and is adjacent to the Jiaolai Basin (Fig. 1b); is therefore considered as a part of the Jiaolai Basin (BGMRSD, 1991).

Lingshan Island is about 40.7 km SE of Qingdao City in Shandong Province of eastern China. It is located in the western region of the Yellow Sea (35°45′1.45″N, 120°09′48.39″E) (Fig. 1b; Fan et al., 2020; Zhang et al., 2020b). Its maximum altitude is 513.6 m, with an area of 7.66 km². Lingshan Island, formed by compression and tilt (Luan et al., 2010), is distinguished by a set
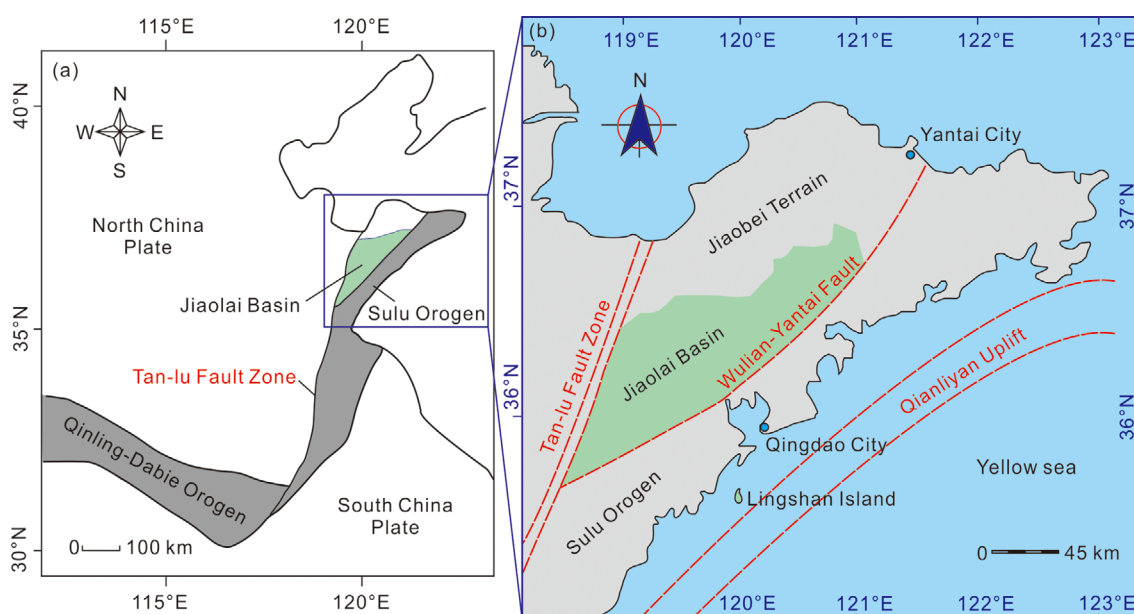
Fig. 1. (a) The Lingshan Island tectonic context (Modified after Zhao et al., 2005); (b) Basic architectural style of Shandong Province's Qingdao region (Modified after Xie et al., 2012).
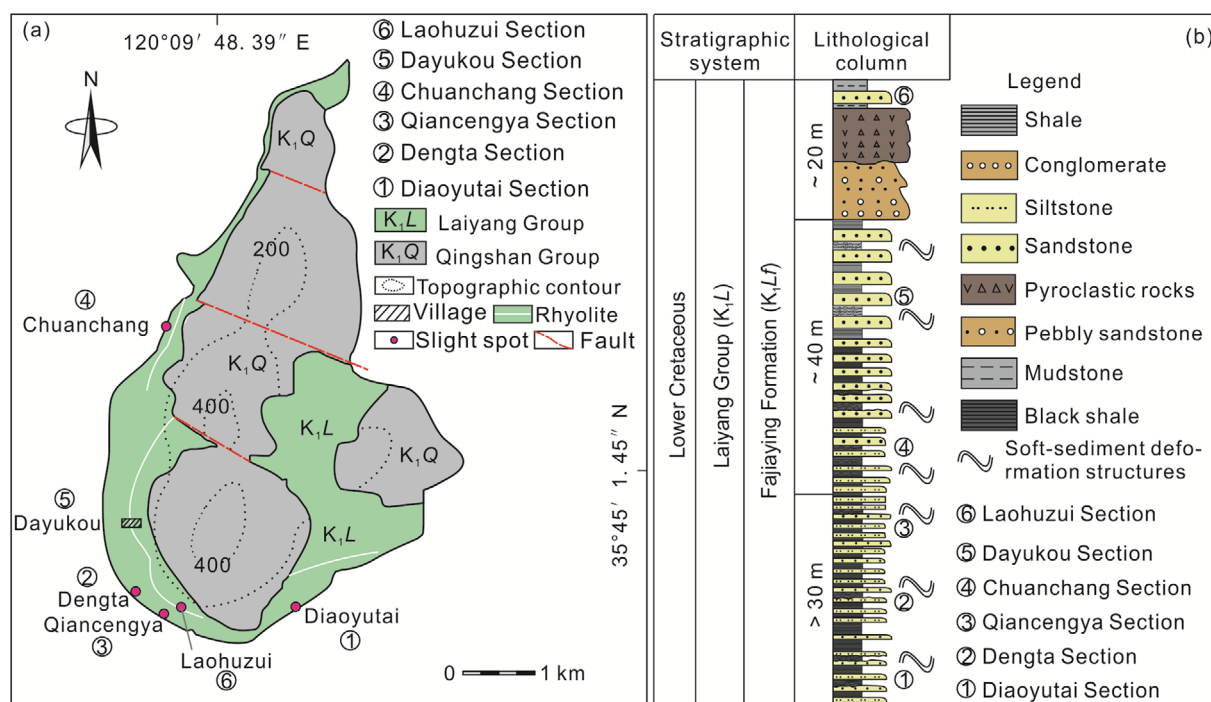
Fig. 2. (a) Lingshan Island geological map schematic showing the locations of the sections under investigation (modified from Zhang et al., 2020b) and (b) Fajiaying Formation lithostratigraphy with stratigraphic positions of the samples (modified from Gao and Li, 2018).

of thick rhyolites (Fig. 2a). Fajiaying Formation (K_1Lf) of the Lower Cretaceous Laiyang Group (K_1L) developed below the thick rhyolites, and the Bamudi Formation (K_1Qb) of the Qingshan Group (K_1Q) developed above the rhyolites (Fig. 2a). Six Fajiaying Formation typical stratigraphic sections are exposed in some villages and slight spots, so these typical sections are named after villages and slight spots. From bottom to top, these stratigraphic sections are the Diaoyutai, Dengta, Qiancengya, Chuanchang, Dayukou and Laohuzui sections (Fig. 2b). The Fajiaying Formation is primarily composed of interbedded black or grey shales, siltstones and sandstones of varying thickness (Fig. 2b), which was deposited in a salinized inland lake (Zhang et al., 2020a, 2020b) with a series of soft-sediment deformation structures caused by seismic activity (Fig. 2b; Lü et al., 2011).

3. MATERIALS AND METHODS

3.1. Sample Collection

As a research object, four continuous sedimentary stratigraphic sections were selected that were based on the west of Lingshan Island (from bottom to top), which include Qiancengya, the Dayukou, the Chuanchang, and the Laohuzui sections. From the Fajiaying Formation (bottom to the top), 30 shale samples were collected. LSD-01 through LSD-30 are the consecutive sample numbers. Seven samples of black shale were associated

with the Qiancengya section, eleven samples of black and grey shales were obtained from the Dayukou section, and eight samples belonged to the Chuanchang section, while the collection of four samples of grey shale was carried out from the Laohuzui section. The time frame and the total number of samples are shown in Figure 3.

3.2. Analytical Methods

For the exposure of the inner uncracked fresh rock's parts, all samples were broken into small fragments. They were crushed in an agate mortar to mesh powder (finer than 200). Analyses of the major, trace, and REE were conducted in Qingdao Sparta Analysis and Testing Co. Ltd. For major elemental analysis, each powder sample was mixed with oxidant (lithium tetraborate) and cosolvent (LiBr) followed by melting and analyzing via an X-ray fluorescence spectrometer (ZSX Primus II) with 1% of accuracy. The major elements were examined using the methods described by Zhang et al. (2020a). Table 1 shows the contents of the major elements. Each sample powder was dissolved in a mixture of ultrapure HF and ultrapure HNO_3 at 200 ℃ for 24 hours for trace-element analysis. Following the powder's digestion, the vials were exposed to air followed by heating at 130 ℃ for three hours to dry the samples. After that, 2 mL of ultrapure HNO_3 and 5 mL of ultrapure water were used to dilute the dried samples. Rare earth and trace elements were measured via an
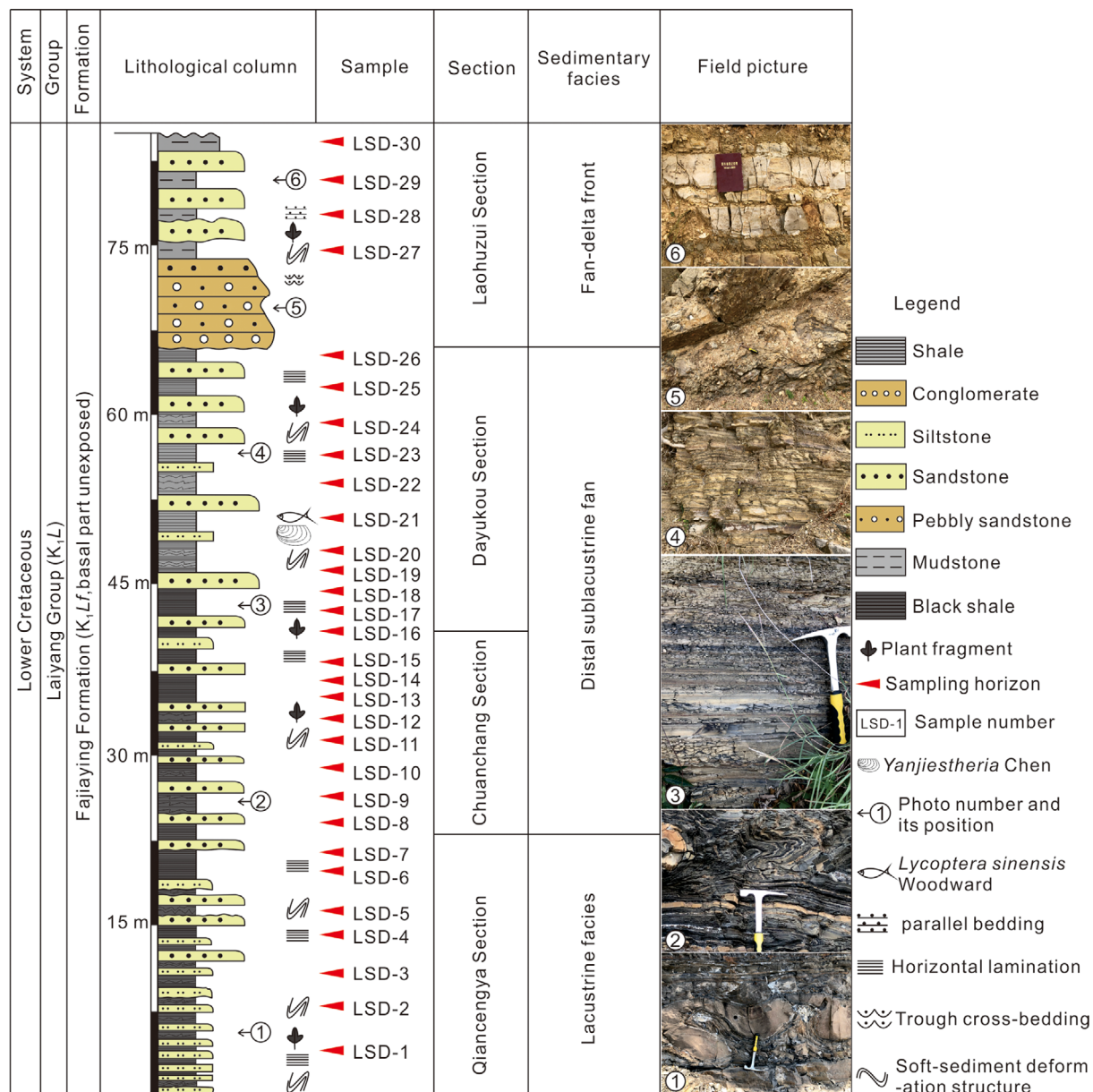
Fig. 3. Lithostratigraphy of the Fajiaying Formation, including photographs of sample locations and representative features of the succession (after Wang, W.X. et al., 2022).

atomic inductively coupled plasma mass spectrometer (ICP-MS; Nu Company, UK). Generally, element concentrations were analyzed with an accuracy of greater than 1%. Zhang et al. (2020c) provides more information on the analytical method for trace and REE. The specific trace and rare earth elements are listed in Table 2.

4. RESULTS

4.1. Petrological and Sedimentary Characteristics

The Qiancengya, Chuanchang and Dayukou outcrops showed

predominantly black shales with some lighter grey ones (Fig. 3). The sandstone and shale from a rock sequence with distinct rhythmic layers, and the outcrop contains numerous soft-sediment deformation structures (Fig. 4a–c). The sandstones were observed as fine-grained with a few siltstones and a thin layer of shale. In the Laohuzui section, the rock sequence was primarily based on earthy brown sandstone and shale with obvious rhythmic layers (Fig. 4d). In addition, a set of the conglomerate was developed in this section, and grains in the conglomerate were found to be angular and splintery (Fig. 4e), indicating the proximity of provenance.

The detrital particles of sandstones in the Fajiaying Formation

Table 1. Results of major-element oxides (wt%) and weathering proxies of shale samples from four typical stratigraphic sections of the Fajiaying Formation (Zhang et al, 2020b; Wang, W.X. et al., 2022)

Samples	Na$_2$O	MgO	Al$_2$O$_3$	SiO$_2$	P$_2$O$_5$	K$_2$O	CaO	TiO$_2$	MnO	Fe$_2$O$_3$	LOI	SUM	Al$_2$O$_3$/MgO	ICV	CIA	CIW
LSD-1	1.62	2.42	17.80	59.85	0.18	4.78	0.74	0.62	0.05	5.50	5.54	99.11	7.57	1.08	67.01	83.26
LSD-2	1.62	2.51	16.95	59.76	0.19	4.36	0.69	0.64	0.07	6.37	5.89	99.04	6.76	1.15	67.37	82.96
LSD-3	2.38	2.33	11.60	59.28	0.24	2.63	5.97	0.48	0.08	5.97	8.39	99.35	4.98	1.81	52.04	59.68
LSD-4	2.43	2.42	14.65	62.78	0.19	3.22	1.64	0.53	0.07	6.48	4.84	99.25	6.06	1.43	59.35	69.13
LSD-5	2.36	2.45	14.57	61.70	0.22	3.12	2.66	0.56	0.04	5.66	7.51	100.85	5.95	1.49	56.66	65.25
LSD-6	2.22	2.65	14.91	59.95	0.15	4.21	3.77	0.41	0.07	4.50	6.18	99.02	5.62	1.48	55.69	67.15
LSD-7	1.46	11.86	5.23	21.49	0.21	1.13	21.52	0.18	0.26	4.53	32.13	100.01	0.44?	7.53?	46.48	52.16
LSD-8	2.55	3.79	11.95	55.16	0.22	2.56	7.62	0.45	0.09	4.53	11.14	100.05	3.15	2.03	51.70	58.77
LSD-9	2.34	1.90	13.38	58.67	0.17	2.93	5.16	0.49	0.07	6.03	7.89	99.02	7.06	1.51	55.17	63.48
LSD-10	1.94	1.89	11.64	48.42	0.16	3.01	13.70	0.42	0.17	2.96	15.07	99.37	6.17	1.45	54.68	64.58
LSD-11	1.88	4.76	12.69	49.41	0.23	2.81	8.16	0.45	0.12	6.25	12.55	99.31	2.67	2.04	57.92	67.29
LSD-12	2.29	3.37	12.00	56.33	0.25	2.63	8.30	0.42	0.14	4.84	9.32	99.89	3.56	1.88	53.62	61.44
LSD-13	2.21	3.89	13.34	56.88	0.19	3.34	5.80	0.63	0.07	5.13	9.21	100.69	3.43	1.87	55.05	64.71
LSD-14	1.74	2.11	14.26	56.21	0.23	3.48	7.06	0.54	0.06	4.20	9.12	99.01	6.75	1.28	60.03	71.37
LSD-15	1.78	2.15	14.34	56.12	0.23	3.48	7.06	0.54	0.06	4.23	9.13	99.11	6.68	1.29	59.79	70.96
LSD-16	2.27	3.74	15.70	58.15	0.22	4.32	1.57	0.87	0.04	6.51	5.76	99.15	4.20	1.63	59.38	72.17
LSD-17	1.83	2.11	14.71	57.56	0.24	3.42	5.63	0.51	0.10	5.46	8.20	99.77	6.98	1.31	60.16	70.92
LSD-18	1.76	2.22	13.28	52.65	0.27	3.01	8.93	0.67	0.08	5.18	11.78	99.83	6.43	1.42	59.40	69.57
LSD-19	2.02	1.93	12.48	56.18	0.35	2.40	9.00	0.60	0.12	4.37	11.47	100.91	6.41	1.42	57.40	65.20
LSD-20	2.44	2.07	14.52	62.94	0.26	3.56	0.84	0.72	0.15	5.92	5.85	99.26	7.40	1.29	62.31	74.70
LSD-21	2.50	1.95	14.25	64.96	0.21	3.21	2.73	0.55	0.08	5.00	4.99	100.43	7.12	1.44	54.92	63.42
LSD-22	2.41	1.96	11.91	50.97	0.20	2.55	11.95	0.43	0.15	4.53	12.66	99.72	4.84	1.61	52.66	60.01
LSD-23	2.36	2.00	11.80	50.56	0.20	2.55	11.98	0.43	0.15	4.49	12.58	99.10	6.07	1.61	52.82	60.30
LSD-24	1.70	2.46	17.08	60.48	0.18	4.34	0.70	0.82	0.13	6.04	6.92	100.87	7.69	1.14	67.16	82.42
LSD-25	2.92	1.94	15.31	64.46	0.25	3.15	0.75	0.58	0.08	6.10	3.81	99.34	7.93	1.21	63.00	73.30
LSD-26	3.85	1.89	15.63	65.38	0.26	2.90	0.67	0.62	0.12	5.98	3.36	100.66	8.26	1.25	60.80	69.27
LSD-27	4.08	1.17	13.95	70.70	0.30	1.97	0.67	0.57	0.14	3.88	2.92	100.35	11.90	1.11	59.86	65.90
LSD-28	4.05	1.15	13.86	70.17	0.29	1.95	0.66	0.56	0.13	3.85	2.90	99.57	12.01	1.11	59.90	65.95
LSD-29	2.09	2.88	16.44	59.15	0.25	3.98	0.88	0.71	0.04	6.76	5.93	99.11	5.71	1.30	65.23	78.72
LSD-30	2.95	2.61	17.04	59.84	0.28	3.83	0.75	0.79	0.02	6.12	4.96	99.18	6.53	1.25	63.71	75.42

Table 2. Trace and rare earth elements (ppm) of the studied shale samples in the Fajiaying Formation

Samples	Rb	Sr	Ba	Pb	Th	U	Zr	Hf	Y	Sc	V	Cr	Cu	Co	Ni	Zn	La	Ce	Pr	Nd	Sm	Eu	Gd	Tb	Dy	Ho	Er	Tm	Yb	Lu
LSD-1	175.89	187.71	1189.47	21.80	20.10	4.12	220.10	5.90	33.09	14.06	117.72	70.07	38.17	6.12	33.71	94.71	65.74	110.57	13.59	49.68	8.99	1.87	7.30	1.16	5.44	1.14	3.06	0.47	2.88	0.44
LSD-2	168.78	190.90	1166.71	25.77	19.72	3.98	223.69	5.86	28.51	12.51	115.61	70.59	39.46	7.98	36.29	123.80	57.47	108.43	11.79	42.92	8.01	1.72	6.33	1.04	4.93	1.04	2.79	0.44	2.72	0.41
LSD-3	89.39	401.28	716.93	54.91	8.89	2.85	216.04	5.44	16.96	8.64	71.22	51.43	43.60	16.53	31.13	90.23	38.14	72.47	7.93	27.91	4.56	1.02	3.68	0.55	2.85	0.61	1.70	0.27	1.71	0.27
LSD-4	119.77	174.51	744.14	20.86	13.94	3.13	218.41	6.07	24.48	11.24	98.84	62.66	23.85	14.10	32.27	124.50	51.33	93.48	10.65	38.86	6.81	1.35	5.33	0.82	4.08	0.89	2.44	0.37	2.43	0.37
LSD-5	139.11	397.77	1101.50	6.32	13.78	3.64	215.42	6.19	23.48	10.40	62.03	40.44	18.99	3.38	15.72	63.80	45.16	85.33	9.80	35.31	6.17	1.14	4.62	0.76	3.82	0.84	2.35	0.37	2.41	0.36
LSD-6	126.15	240.62	722.52	16.68	15.47	3.31	215.39	5.92	28.35	12.27	94.47	68.47	25.25	7.18	28.34	59.49	43.14	80.54	9.72	35.35	6.60	1.32	5.50	0.91	4.62	0.97	2.78	0.44	2.75	0.41
LSD-7	40.94	825.62	395.50	10.14	5.37	2.83	150.21	2.64	12.97	4.76	74.66	27.63	11.68	4.51	11.76	18.74	16.57	33.59	3.76	13.91	2.67	1.07	2.36	0.38	1.92	0.40	1.11	0.17	1.05	0.16
LSD-8	93.85	370.77	812.27	15.80	10.16	2.36	184.06	4.90	21.67	9.42	80.22	53.33	27.66	8.77	23.50	60.62	35.15	68.37	7.70	28.27	5.07	1.16	4.37	0.70	3.54	0.75	2.01	0.31	2.00	0.30
LSD-9	108.13	362.52	724.99	38.74	13.33	2.66	204.06	5.34	23.34	10.98	84.62	61.20	34.24	12.95	31.30	92.81	47.46	86.59	10.09	36.63	6.71	1.36	5.18	0.82	4.04	0.86	2.39	0.37	2.37	0.36
LSD-10	107.85	1311.43	741.99	9.52	12.43	2.91	160.73	4.32	26.07	12.02	93.10	61.61	26.89	10.36	25.94	117.20	41.25	76.04	8.77	32.07	6.11	1.45	5.03	0.85	4.24	0.93	2.48	0.39	2.43	0.38
LSD-11	107.08	279.59	686.37	16.02	10.51	3.56	155.56	3.91	26.89	14.76	141.47	76.02	38.17	16.95	32.09	96.71	45.15	88.28	10.01	37.05	6.93	1.40	5.74	0.92	4.37	0.94	2.46	0.38	2.38	0.36
LSD-12	84.32	470.61	718.00	22.22	12.16	2.93	175.87	4.31	23.36	8.29	69.08	44.65	30.84	13.63	28.16	87.14	43.33	84.93	9.50	35.00	6.35	1.29	5.10	0.82	4.02	0.85	2.38	0.36	2.18	0.32
LSD-13	154.21	175.99	1487.58	29.10	19.73	3.73	208.42	6.59	28.26	19.52	99.13	58.97	41.44	18.27	39.75	74.59	64.53	145.25	13.12	49.28	8.52	1.81	7.43	1.13	5.92	1.10	3.15	0.45	2.94	0.45
LSD-14	131.96	338.63	730.94	10.95	13.61	3.06	178.76	4.56	24.63	11.09	98.73	66.37	23.92	4.44	31.84	65.98	46.64	87.27	9.93	36.24	6.68	1.33	5.39	0.85	4.22	0.90	2.42	0.39	2.42	0.37
LSD-15	133.61	336.23	767.02	10.81	13.35	3.09	179.61	4.44	24.31	11.46	100.32	66.89	24.30	4.65	26.23	67.65	47.61	87.88	10.07	36.67	6.78	1.35	5.47	0.87	4.19	0.90	2.49	0.38	2.37	0.35
LSD-16	96.64	189.77	937.64	28.73	10.57	2.36	193.68	5.82	21.18	18.46	95.79	60.14	36.90	17.45	34.13	100.29	53.84	113.25	12.36	47.64	7.68	1.47	6.34	0.95	4.84	0.89	2.64	0.39	2.53	0.37
LSD-17	135.63	213.17	756.80	28.67	14.29	3.67	164.18	4.17	26.55	10.15	97.72	67.28	36.42	9.53	37.49	98.41	45.73	86.86	10.02	36.94	6.96	1.36	5.71	0.91	4.65	0.96	2.61	0.40	2.51	0.37
LSD-18	106.38	329.05	561.97	9.62	11.98	4.83	156.39	4.60	22.03	12.95	101.39	55.58	32.71	7.24	33.73	83.19	46.78	93.64	10.75	39.01	6.59	1.34	5.65	0.85	4.36	0.80	2.38	0.34	2.24	0.33
LSD-19	124.53	344.82	590.49	19.13	10.30	2.71	164.05	4.88	19.08	10.64	74.25	41.85	20.15	7.79	17.64	54.93	41.08	88.31	9.75	35.81	6.28	1.22	5.33	0.81	4.17	0.77	2.28	0.33	2.21	0.32
LSD-20	103.21	479.82	539.42	13.46	11.75	5.55	170.11	4.77	25.88	13.71	95.97	49.22	25.73	5.65	22.29	49.77	45.96	85.90	10.82	40.43	7.40	1.65	6.52	1.01	5.34	0.99	2.81	0.40	2.60	0.39
LSD-21	115.71	217.63	927.17	19.10	12.04	2.70	209.15	5.24	23.70	10.12	77.93	69.98	29.79	5.62	25.04	51.03	52.18	95.75	11.02	40.33	7.11	1.50	5.44	0.86	4.15	0.87	2.40	0.36	2.25	0.34
LSD-22	86.42	614.79	789.81	13.94	12.88	5.62	169.64	4.34	27.86	10.17	81.87	51.73	32.75	8.23	26.73	46.93	44.73	81.91	9.40	34.64	6.60	1.65	5.66	0.91	4.74	1.03	2.68	0.43	2.59	0.40
LSD-23	91.89	623.91	826.13	17.04	13.31	5.71	178.67	4.52	28.72	11.26	84.39	54.25	33.11	8.25	26.87	49.43	45.57	83.66	9.66	35.71	6.62	1.65	5.76	0.94	4.82	1.04	2.75	0.43	2.69	0.42
LSD-24	112.05	144.79	1173.89	14.80	16.18	4.48	262.23	7.28	27.96	17.50	82.48	54.03	32.64	6.52	26.23	97.35	45.92	99.92	11.02	41.81	7.62	1.66	6.96	1.09	5.92	1.11	3.25	0.48	3.14	0.47
LSD-25	95.97	198.53	1252.64	24.48	11.07	1.76	204.72	5.23	27.62	10.42	87.54	64.90	30.87	13.46	34.25	95.88	58.74	107.44	12.80	46.89	8.45	1.78	6.81	1.04	5.13	1.06	2.86	0.43	2.70	0.40
LSD-26	88.12	222.64	1225.45	24.45	11.62	1.87	216.61	5.45	28.52	13.42	93.71	65.34	31.27	13.96	32.89	98.28	60.23	111.58	13.16	49.16	9.10	1.89	7.11	1.10	5.29	1.10	2.90	0.44	2.75	0.41
LSD-27	61.70	182.36	977.01	24.18	8.73	1.88	207.83	4.98	22.81	11.80	73.45	48.70	25.08	8.83	27.84	72.12	60.07	98.53	12.55	45.77	7.86	1.62	6.03	0.90	4.14	0.88	2.41	0.35	2.31	0.34
LSD-28	61.63	174.49	991.57	23.93	8.15	1.86	218.15	5.13	22.58	11.47	73.48	49.74	24.35	8.91	21.27	78.49	59.33	96.54	12.36	44.74	7.62	1.60	5.85	0.88	4.09	0.84	2.30	0.36	2.24	0.33
LSD-29	140.79	230.12	1286.83	22.49	14.38	2.41	223.31	6.06	30.47	12.07	123.14	72.81	41.74	8.37	34.96	106.90	60.10	109.09	12.76	47.18	8.57	1.74	6.90	1.06	5.24	1.12	2.97	0.46	2.89	0.43
LSD-30	122.36	193.28	1256.48	23.28	12.76	2.45	219.61	5.81	23.37	12.72	149.22	73.68	37.39	6.82	29.04	80.07	64.73	114.15	13.11	47.40	7.99	1.75	6.04	0.90	4.10	0.86	2.44	0.38	2.39	0.36
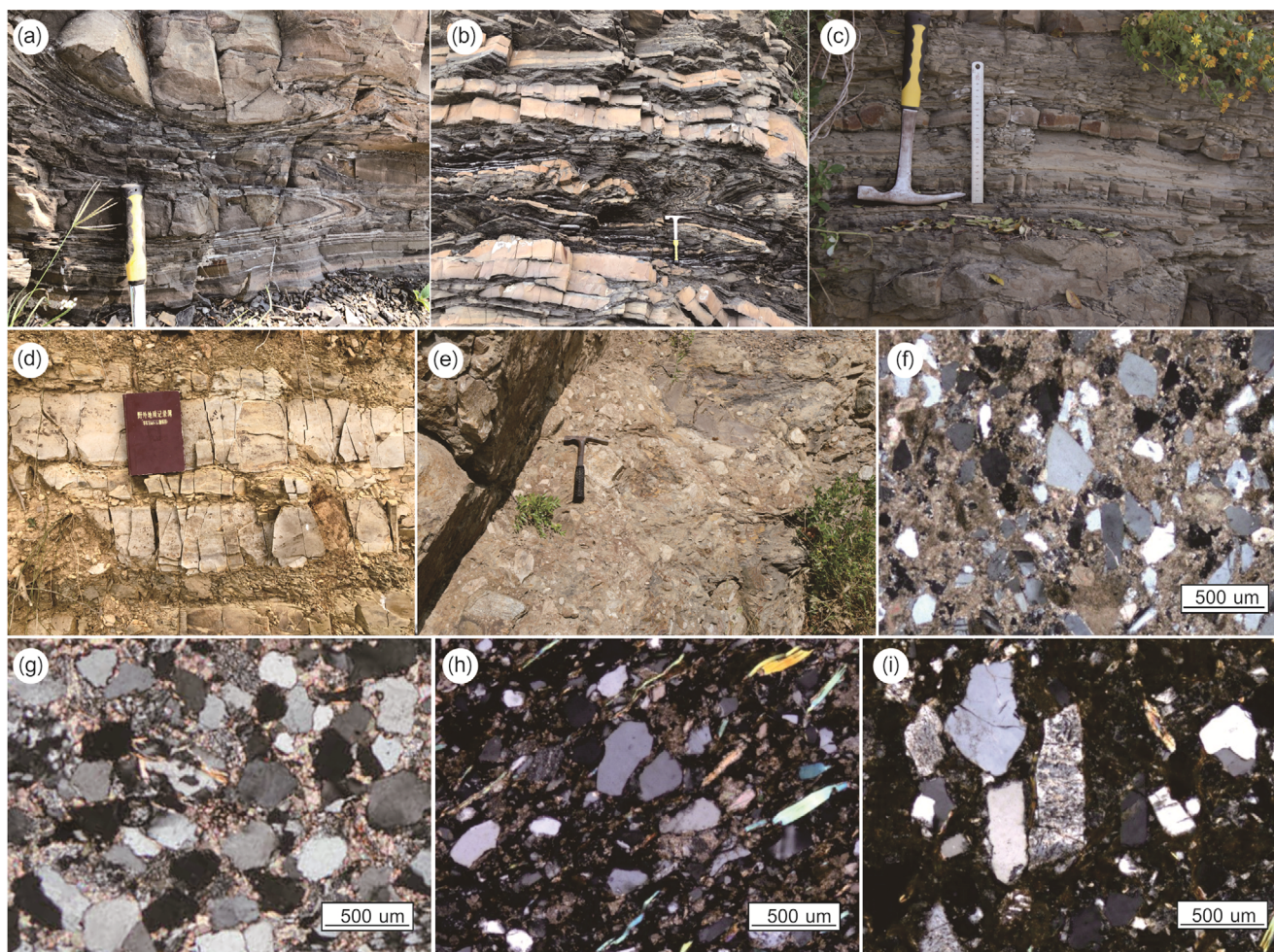
Fig. 4. Sedimentary characteristics in the outcrop on Lingshan Island and photographs of the sandstones' textural characteristics in thin sections taken with cross-polarized light. (a) The rhythmic layers by sandstone and shale in the Qiancengya section; (b) Chuanchang section; (c) Dayukou section; (d) The rock sequence by sandstone and shale in the Laohuzui section; (e) Conglomerate of the Laohuzui section; (f–i) Photomicrographs of sandstones from (f) the Chuanchang section, (g) the Dayukou section, (h) the Qiancengya section and (i) the Laohuzui section, presenting the grain's rounding and sorting. Grains were found to be angular and splintery, indicating the nearness of provenance.

were primarily angular to subangular and poorly sorted (Fig. 4f–h). The larger grains were found to be angular and splintery, while the smaller grains were round to sub-rounded (Fig. 4f–h), indicating the nearness of provenance. It is worth noting that the sandstone particles in all sections had a clear preferred orientation (Fig. 4f–h), showing the direction of water flow.

4.2. Geochemistry

4.2.1. Major oxides

The SiO_2 content ranged from 48.42 to 70.17 wt% while the range of more stable elements i.e., TiO_2 and Al_2O_3 contents was found to be 0.41–0.87 and 11.6–18.80 wt%. While the less stable elements i.e., CaO, Na_2O, and K_2O are varied ranging from 0.66 to 11.98 wt%, 1.62 to 4.08 wt%, and 1.95 to 4.78 wt%, respectively. When compared to post-Archean Australian shales

(PAAS; Fig. 5a), the samples exhibited higher average Na_2O, CaO, and MgO content. In general, the major element contents were lower than the upper continental crust (UCC) values, except for CaO (Fig. 5b).

Strong relationships between SiO_2 with MgO (Fig. 6a) and CaO (Fig. 6b) suggested that carbonate may have originated from the same source. The TiO_2, and K_2O have a strong positive correlation with Al_2O_3 (Fig. 6c, d), indicating that these elements are probably hosted within the clay minerals.

4.2.2. Trace and rare earth elements

The trace elements were normalized by PAAS (Fig. 7a) and UCC (Fig. 7b), respectively. Compared to the post-Archean Australian shales, the Sr content of the shale was enriched (mean: 347.44 ppm), similar to UCC. The content of Ba (between 539.42 and 1487.58 ppm, with an average of 893.31 ppm) was significantly
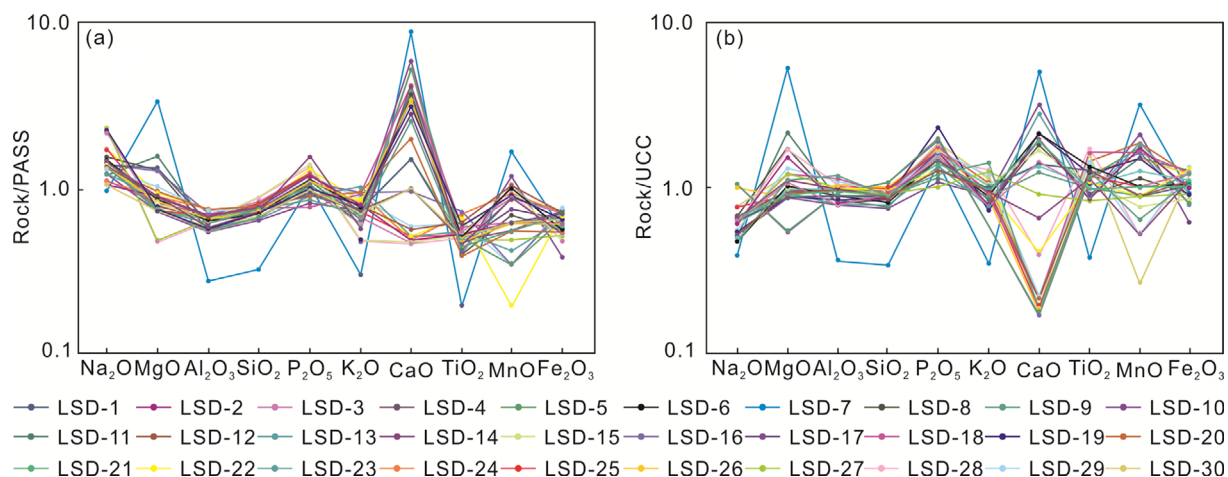
Fig. 5. Spider plot of major element compositions of Fajiaying Formation shale samples, normalized against PAAS (a) and UCC (b). Data from Taylor and McLennan are used for UCC and PAAS (1985).
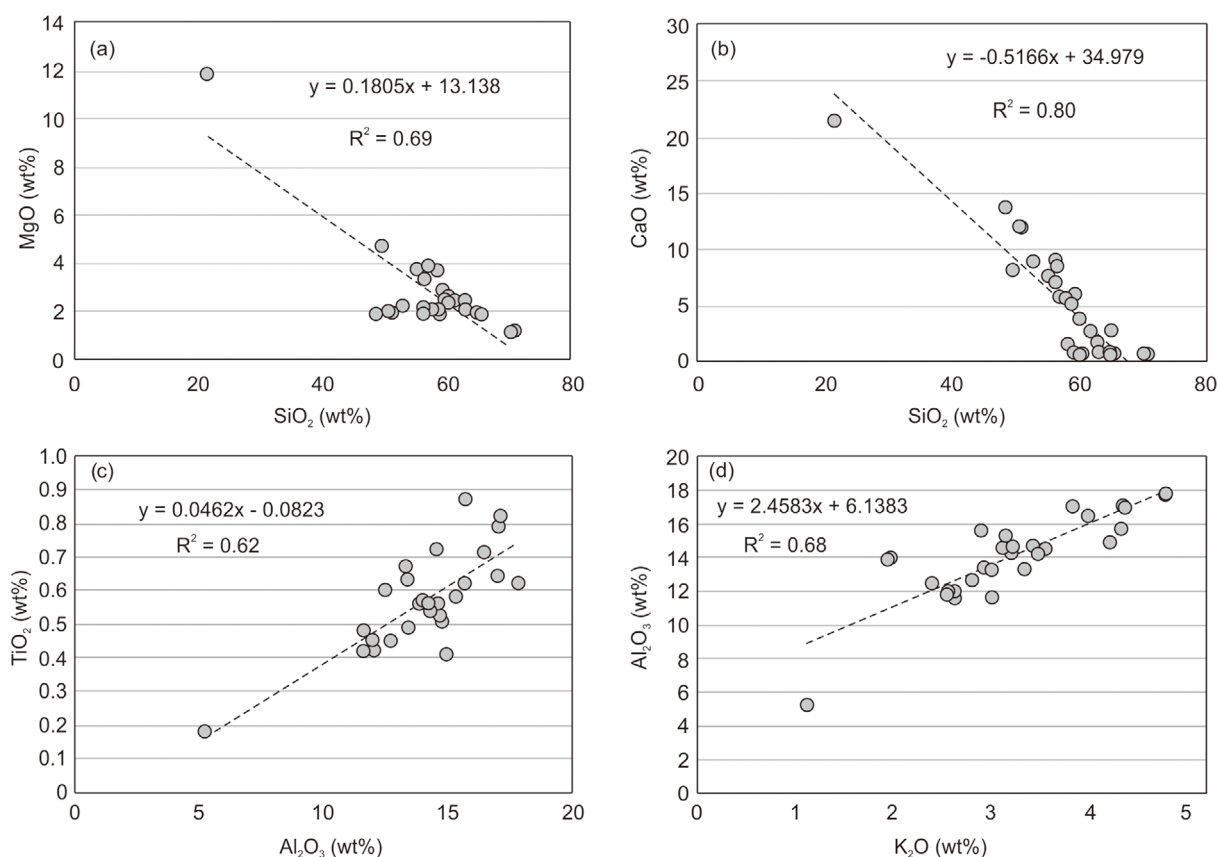

Fig. 6. Cross-plots of major elements for the shale samples studied.

higher than that of the UCC and PAAS. The Zr content was similar to that of the UCC but slightly lower than that of the PAAS. With an average content of 30.65 ppm, Cu abundance was found to be similar to that of the UCC, but lower than that of the PAAS. The Pb, U, and Y contents are less than that of the UCC but similar to PAAS. The contents of Rb and Th are less

than those of the PAAS but higher than the PAAS. The other elements (Sc, V, Cr, Co and Ni) are relatively depleted in the UCC, and are also significantly lower than the PAAS.

Ratios of the specific trace and rare earth elements are listed in Table 3. The total REE content (ΣREE) of the studied samples was observed over a range of 166.40 to 265.20 ppm (average =
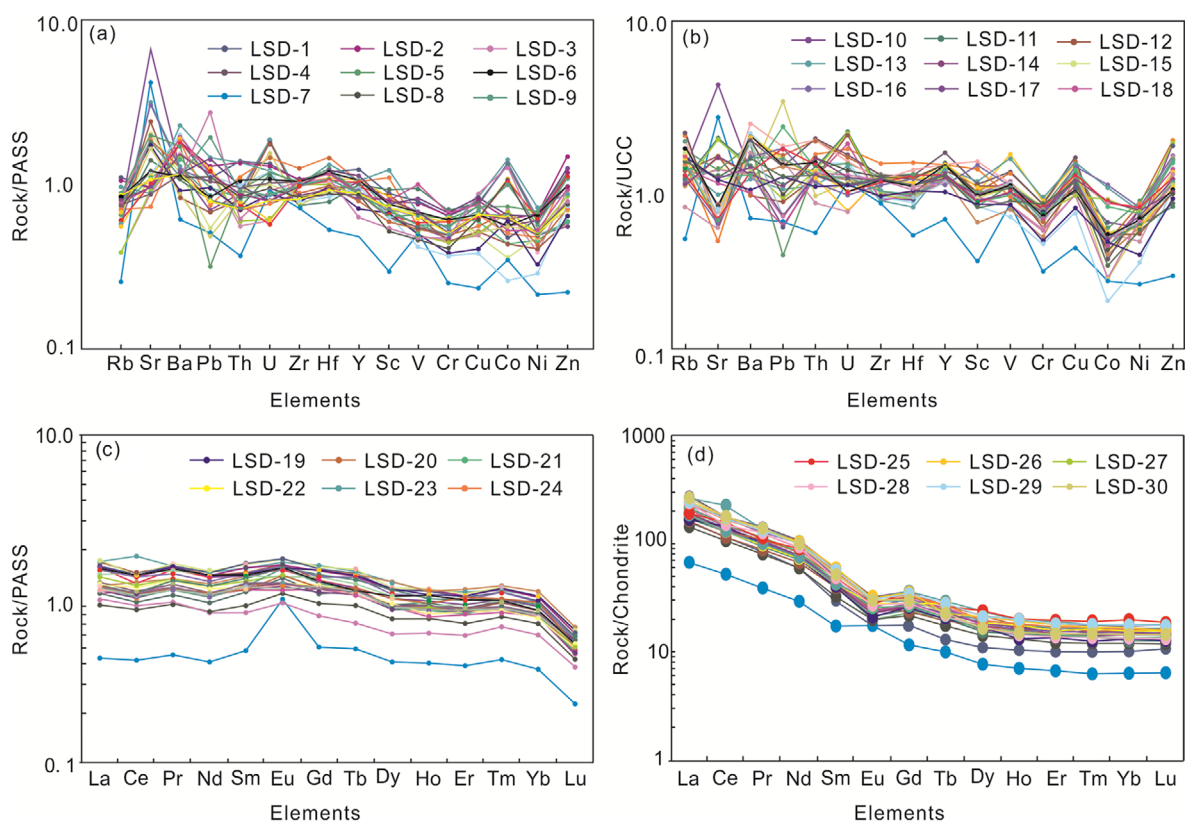
Fig. 7. Spider plot of trace element compositions of Fajiaying Formation shale samples, normalized against (a) PAAS and (b) UCC. (c) PAAS and (d) chondrite normalized Rare Earth Element (REE) plots for investigated shales from the Fajiaying Formation. Chondrite normalization values are from Taylor and McLennan (1985).

216.62 ppm) with the (ΣLREE/ΣHREE) ratio covering a range of 9.61 to 15.15 (average = 11.47). The Eu anomaly (Eu/Eu*) ranges from 0.61 and 0.81 (average = 0.73). Figure 7a depicts the PAAS-normalized REE curves (Taylor and McLennan, 1985). Weak enrichment in LREE (La, Pr, Ce, Sm, Nd, Eu) and a nearly flat distribution of HREE (Tb, Gd, Dy, Er, Ho, Tm, Nd) can be seen in the PAAS-normalized REE patterns of the studied samples (Fig. 7a). The abundance of LREE suggests that the REE primarily come from detrital sources. Shale-like patterns can be seen in the PAAS-normalized REE patterns of the studied samples, but no obvious Eu anomaly was visible (Fig. 7c). The studied samples' chondrite-normalized REE patterns typically displayed a considerably inclined trend with a negative Eu anomaly, while the HREE exhibited a flat trend (Fig. 7d). All patterns exhibited pronounced fractionations between the LREE (ranges from 152.03 to 302.62 ppm, average of 216.62 ppm) and HREE (ranges from 14.64 to 21.43 ppm, average of 17.33 ppm). The studied shales yield La_N/Yb_N, La_N/Sm_N, and Gd_N/Yb_N ratios of 9.50–18.29, 3.80–5.27, and 1.29–1.97, respectively. The values show that LREEs are abundant and HREEs are scarce in the analyzed samples.

5. DISCUSSION

## 5.1. Factors Affecting the Clastic Sediment Chemistry

Numerous factors, such as post-depositional alteration, and mechanical sorting and recycling during sediment transport and deposition can influence clastic sediment chemistry (e.g., Nesbitt and Young, 1982; Taylor and McLennan, 1985; McLennan et al., 1993; Fedo et al., 1995). When analyzing the geochemistry of clastic sediments, it is indispensable to identify the influence of these factors.

5.1.1. Post-depositional alteration process

The sedimentary rocks' geochemistry can be modified by post-depositional alteration. Primarily, silicification and K-metasomatism are two essential post-depositional geological processes (Cullers et al., 1993; Fedo et al., 1995). During the silicification process, certain elements can be removed (i.e., Ca, Mg and Na), while Si and, on occasion, K can be added (Cullers, 1995). The studied shale samples exhibited narrow K_2O/Na_2O and SiO_2/Al_2O_3 ranges, suggesting post-depositional K-metasomatism or silicification was insignificant (Fig. 8a). Although the samples

Table 3. Ratios of the specific trace and rare earth elements for the shale samples

Samples	La_N/Yb_N	La_N/Sm_N	Gd_N/Yb_N	Zr/Hf	Th/U	Th/Sc	Zr/Sc	Al/Si	K/Si	Rb/Sr	Sr/Cu	ΣREE	ΣLREE	ΣHREE	ΣLREE/ΣHREE	Eu/Eu*
LSD-1	15.44	4.61	1.49	37.32	4.88	1.43	15.65	0.29	0.10	0.94	4.92	269.89	250.45	19.89	12.59	0.77
LSD-2	14.28	4.51	1.29	38.19	4.95	1.58	17.88	0.28	0.09	0.88	4.84	247.63	230.34	17.70	13.01	0.81
LSD-3	9.50	5.27	1.70	39.68	3.12	1.03	25.00	0.25	0.06	0.22	9.20	166.40	152.03	14.64	10.38	0.61
LSD-4	14.29	4.74	1.78	36.00	4.46	1.24	19.43	0.24	0.07	0.69	7.32	218.82	202.46	16.74	12.10	0.66
LSD-5	12.65	4.61	1.55	34.81	3.78	1.33	20.72	0.23	0.06	0.35	20.94	198.08	182.91	15.54	11.77	0.63
LSD-6	10.60	4.12	1.62	36.40	4.67	1.26	17.56	0.31	0.09	0.52	9.53	194.65	176.67	18.39	9.61	0.65
LSD-7	5.45	3.91	0.93	56.96	1.90	1.13	31.54	0.23	0.07	0.05	70.67	79.97	71.58	8.56	8.36	1.27
LSD-8	11.88	4.36	1.77	37.58	4.31	1.08	19.54	0.23	0.06	0.25	13.40	159.40	145.72	13.98	10.42	0.74
LSD-9	13.53	4.46	1.77	38.18	5.01	1.21	18.58	0.24	0.06	0.30	10.59	204.88	188.83	16.40	11.51	0.68
LSD-10	11.46	4.25	1.68	37.19	4.27	1.03	13.37	0.28	0.08	0.08	48.77	182.05	165.70	16.72	9.91	0.78
LSD-11	12.79	4.10	1.95	39.83	2.95	0.71	10.54	0.24	0.07	0.38	7.32	206.00	188.81	17.55	10.76	0.66
LSD-12	13.43	4.30	1.90	40.79	4.15	1.47	21.21	0.24	0.06	0.18	15.26	196.12	180.40	16.04	11.25	0.67
LSD-13	14.85	4.77	1.50	31.63	5.29	1.01	10.67	0.27	0.07	0.88	4.25	302.62	282.50	20.57	13.73	0.76
LSD-14	13.00	4.39	1.80	39.22	4.44	1.23	16.12	0.26	0.08	0.39	14.16	204.70	188.10	16.97	11.08	0.66
LSD-15	13.58	4.42	1.87	40.50	4.32	1.17	15.67	0.26	0.08	0.40	13.84	207.03	190.35	17.03	11.18	0.65
LSD-16	14.41	4.41	1.97	33.30	4.47	0.57	10.49	0.30	0.09	0.51	5.14	254.60	236.23	18.75	12.60	0.63
LSD-17	12.34	4.14	1.85	39.35	3.90	1.41	16.18	0.25	0.08	0.64	5.85	205.63	187.87	18.13	10.36	0.64
LSD-18	14.09	4.47	1.97	33.99	2.48	0.92	12.08	0.25	0.07	0.32	12.79	214.56	198.12	16.76	11.82	0.67
LSD-19	12.57	4.12	1.96	33.64	3.80	0.97	15.42	0.21	0.05	0.36	11.57	198.35	182.45	16.22	11.25	0.63
LSD-20	11.94	3.91	1.91	35.65	2.12	0.86	12.41	0.27	0.07	0.22	14.65	211.44	192.16	19.66	9.77	0.73
LSD-21	15.66	4.62	1.96	39.91	4.47	1.19	20.68	0.24	0.06	0.53	6.57	224.22	207.88	16.68	12.46	0.71
LSD-22	11.66	4.27	1.77	39.08	2.29	1.27	16.68	0.23	0.06	0.14	18.84	196.97	178.94	18.43	9.71	0.81
LSD-23	11.43	4.33	1.73	39.50	2.33	1.18	15.87	0.23	0.06	0.15	20.21	201.30	182.87	18.85	9.70	0.80
LSD-24	9.90	3.80	1.54	36.02	3.61	0.92	14.99	0.28	0.09	0.77	4.43	228.90	207.94	21.43	9.70	0.73
LSD-25	14.68	4.38	1.74	39.12	6.27	1.06	19.64	0.22	0.06	0.48	9.85	255.14	236.09	19.45	12.14	0.74
LSD-26	14.82	4.17	1.51	39.72	6.21	0.87	16.14	0.20	0.06	0.40	7.12	263.81	245.13	19.10	12.83	0.78
LSD-27	17.60	4.81	1.91	41.72	4.63	0.74	17.62	0.15	0.04	0.34	7.27	242.82	226.40	16.76	13.51	0.72
LSD-28	17.86	4.90	1.93	42.50	4.39	0.71	19.02	0.15	0.04	0.35	7.17	238.27	222.20	16.40	13.55	0.73
LSD-29	14.04	4.41	1.65	36.83	5.96	1.19	18.50	0.26	0.09	0.61	5.51	259.08	239.44	20.08	11.93	0.71
LSD-30	18.29	5.10	1.70	37.79	5.21	1.00	17.26	0.24	0.08	0.63	5.17	265.20	249.12	16.44	15.15	0.79
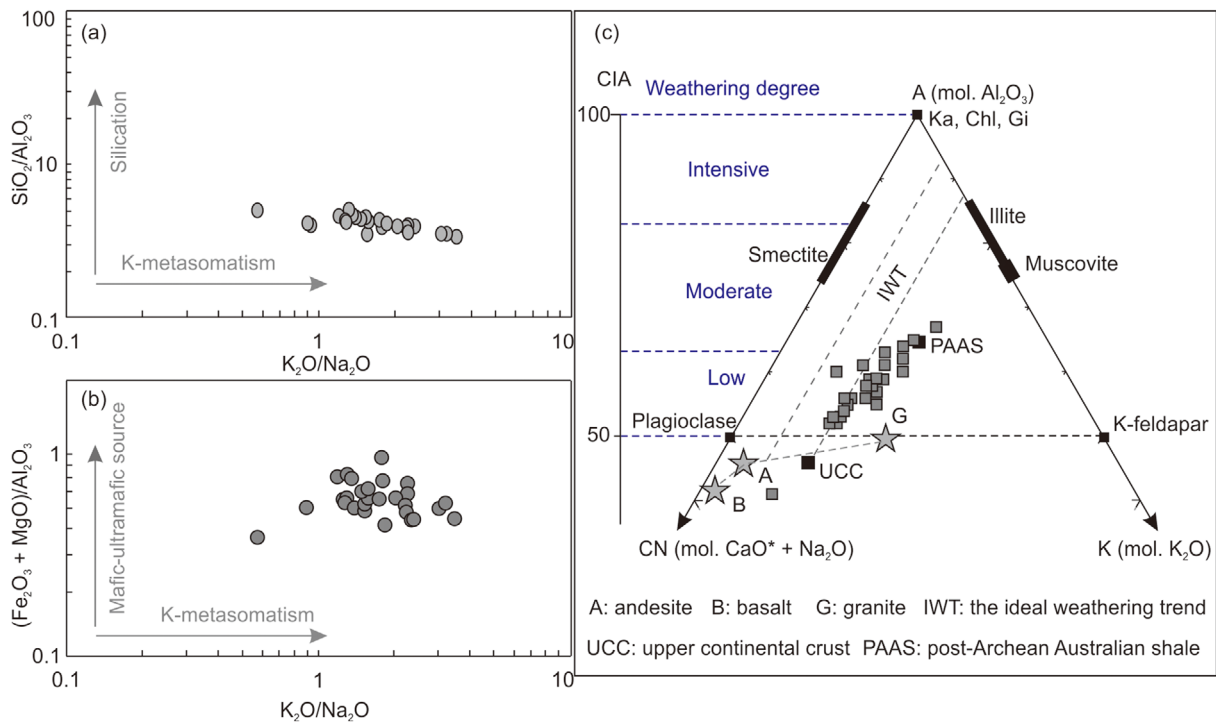
Fig. 8. (a) $(Fe_2O_3 + MgO)/Al_2O_3$ vs. K_2O/Na_2O; (b) SiO_2/Al_2O_3 vs. K_2O/Na_2O; (c) A-CN-K diagrams for the Fajiaying Formation shales sedimentary rocks.

have varying K_2O/Na_2O ratios, this is most likely due to mixed detrital provenance rather than K-metasomatism (Fig. 8b). Ternary A-CN-K diagram (Fig. 8c) displays that the majority of studied samples fall within the expected weathering trends, suggesting negligible K-metasomatism.

5.1.2. Sedimentary recycling and hydrodynamical sorting

Elements with low mobility and insolubility play an essential role as proxies during the recycling process (Fathy et al., 2021). Therefore, the distribution of Hf, Zr, Sc, and Th has been used

to track the sedimentary recycling role within the sediments (e.g., Mclennan et al., 1993; Absar, 2021; Wang, W.X. et al., 2022). During sedimentary recycling, there was a significant change in the Th/Sc ratio with a significant increase in Zr/Sc ratio (McLennan, 1989; McLennan et al., 1993). Hence, the assessment of sedimentary sorting as well as recycling can be carried out by using Th/Sc and Zr/Sc ratios. The studied shales' geochemical composition was found to be regulated by the composition of the source rather than sediments recycling, as evidenced by the fact that the majority of studied samples have varying Zr/Sc and Th/Sc ratios and are clustered along the primary compositional trend
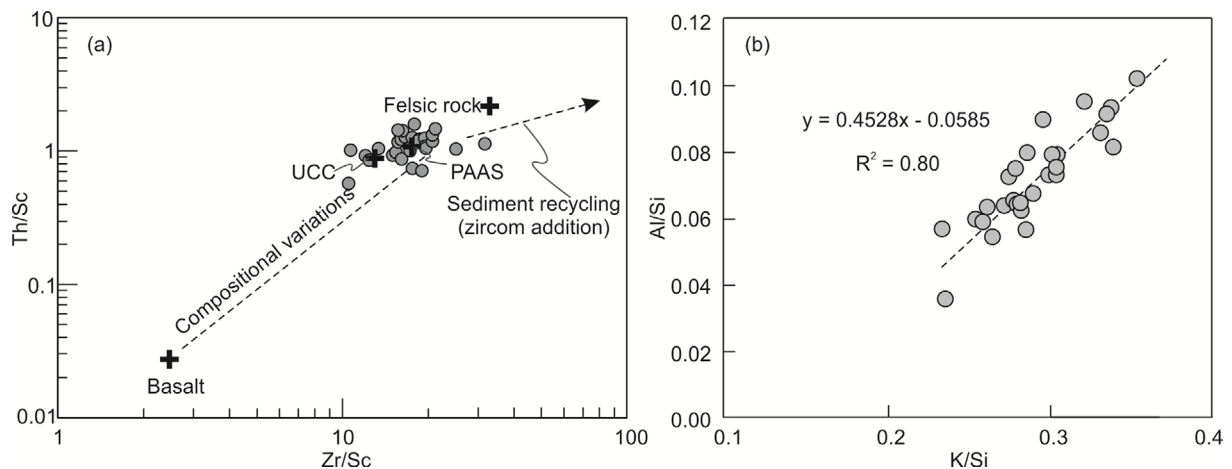
Fig. 9. Evaluation of sedimentary recycling sources for the Early Cretaceous shales in the Fajiaying Formation using (a) Zr/Sc vs. Th/Sc plot and (b) Al/Si vs. K/Si plot (modified after Wang, W.X. et al., 2022).

(Fig. 9).

The detrital particles of sandstones in the Fajiaying Formation present poor sorting and roundness, and high rock fragments and feldspar contents (Fig. 4f–i), indicating the immaturity of the sediments. Sediment recycling and sediment maturity in the study area are also evaluated using the shale's index of compositional variability (ICV). The formula for determining the ICV is as follows (the oxides were calculated by molecular proportions):

$$ICV = (K_2O + Fe_2O_3 + Na_2O + MgO + CaO + MnO + TiO_2)/Al_2O_3 \text{ (Cox et al., 1995)}.$$

The ICV value for first-cycle products in tectonically active regions is typically greater than 1 (Van de Kamp and Leake, 1985) while it varied over a range of 1.18 and 3.34 for the shales in the Fajiaying Formation (Table 1). These values are significantly greater than the PAAS (0.80), which indicates that the shales are first-cycle and compositionally immature with no hydrodynamical sorting effect.

The Al/Si and K/Si ratios serve as indicators of sediment sorting (Fathy et al., 2021; Wang, W.X. et al., 2022). The value of these ratios in fine-grained sediments is typically higher than those in coarse-grained sediments (Fathy et al., 2021). The Al/Si ratio varies between 0.15 and 0.31, whereas the K/Si ratio ranges between 0.04 and 0.10 (Table 2). The ratios of Al/Si and K/Si are correlated strongly in this study (R^2 = 0.80; Fig. 9b), which confirms that there is no hydrodynamical sorting effect. Furthermore, the density, size, and shape of grain are the primary factors that influence sorting (Fathy et al., 2021; Wang, W.X. et al., 2022). The degree to which sedimentary sorting affects clastic grain can be inferred from its size, density, and shape. The sedimentary features of the Fajiaying Formation are the rock sequences with obvious rhythmic layers of sandstone
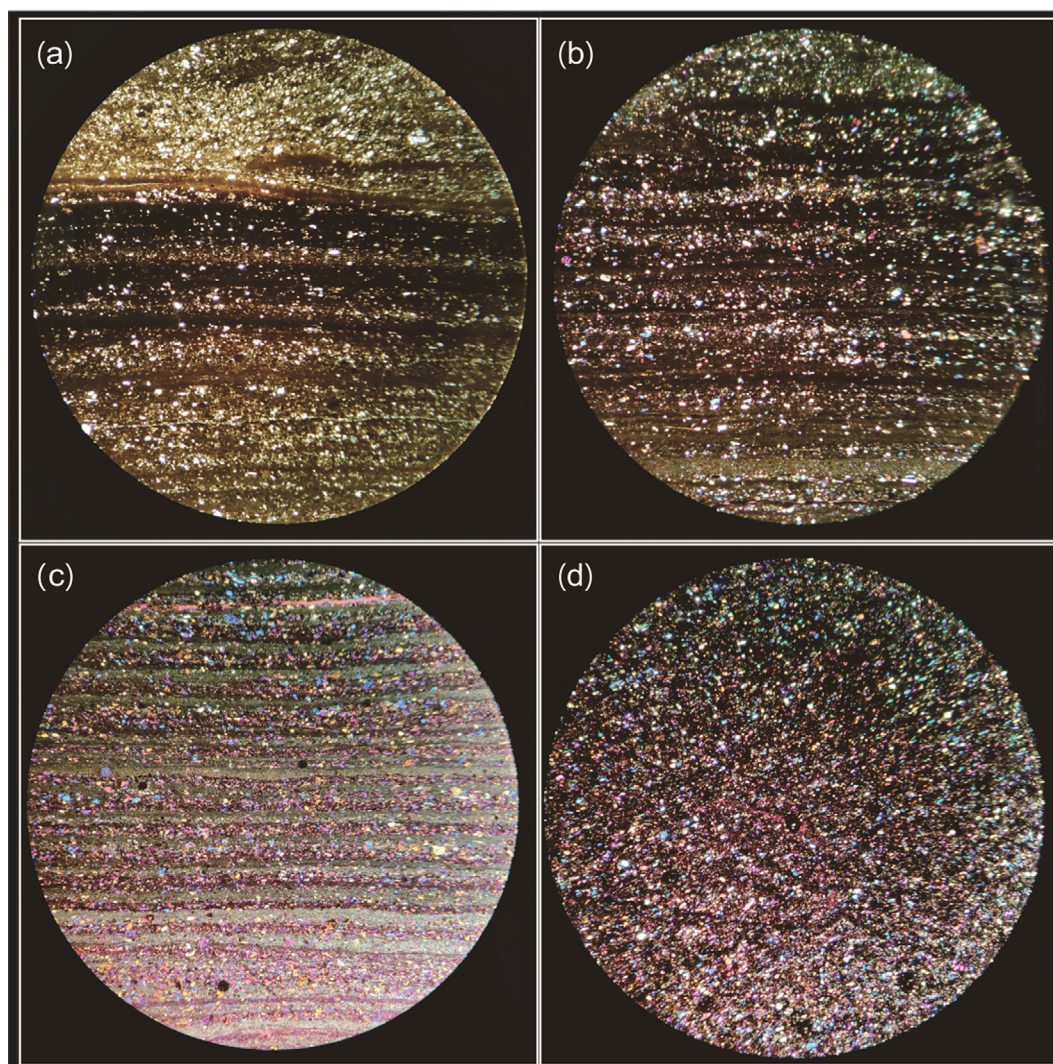
Fig. 10. Thin-section photomicrographs showing the textural features of shales from the Qiancengya (a), Chuangchang (b), Dayukou (c), and Laohuzui (d) sections. The diameter of the visual field is 1 mm.

and shale (Fig. 4a–d). Here, thin-section photomicrographs (Fig. 10) of shale from four different sections were used to distinguish the hydrodynamic sorting. Photos of shale from sections other than Laohuzui revealed distinct sedimentary bedding and uniform clastic particle distribution (Fig. 10), indicating weak hydrodynamic sorting.

The geochemistry of the shales would be utilized to infer the sedimentary history of the source area (e.g., provenance, tectonic setting and paleoweathering conditions) after ensuring that the shale chemistry in the area of the study has not been influenced by post-depositional alteration, mechanical sorting, and recycling.

5.2. Provenance Characteristics

The concentrations of trace, major, and REEs of sediments can provide valuable information about unknown provenance (e.g., Madhavaraju et al., 2016; Armstrong-Altrin et al., 2017). For instance, some elements (Ti, Al, and Zr) are insoluble under low temperatures in aqueous solutions, which can be used to determine the parent rock's composition. On the bivariate plot of Al_2O_3 and TiO_2, the studied shale samples are primarily located in the granite field (Fig. 11a) confirming that the samples studied in this study originated from felsic igneous rocks, as suggested by the TiO_2 and Zr binary diagram (Fig. 11b). The studied samples are plotted close to the granite provenance field on the Co/Th and La/Sc discrimination diagrams (Fig. 11c), indicating the felsic igneous rocks as the regional source. The binary diagram of Hf and La/Th (Fig. 11d) further supports the above result. Additionally, K_2O versus Rb diagram also exhibited a similar conclusion (Fig. 11e; after Floyd et al., 1989), where most of the samples were plotted within the range of intermediate to acidic rocks along the magmatic trend.

Roser and Korsch's (1988) discriminant function diagram is extensively utilized in sedimentary provenance studies. With the help of this diagram, it is possible to distinguish between mafic (P1), intermediate (P2), felsic (P3), and recycled quartzose (P4) provenances. Most samples in our study were plotted in the felsic igneous provenance field (Fig. 11f), indicating the majority of sediments were based on felsic rock types. Furthermore, the studied shale samples plot in the granitic rocks field on the [La/Yb]/ΣREE diagram (Fig. 11g; after Floyd and Leveridge, 1987).

Furthermore, the relative size and REE patterns of Eu anomaly can be used to infer the origins of sedimentary rocks (Taylor and McLennan, 1985). It has been found that negative Eu anomalies and higher LREE/HREE ratios are related to felsic igneous rocks, while lower ratios and slightly positive anomalies can be observed in mafic igneous rocks (Cullers, 1994; Cullers and Podkovyrov, 2000; Armstrong-Altrin et al., 2017). The studied

shale samples contain higher LREE/HREE ratios (9.61–15.15, average, 11.47) and slight Eu anomalies, supporting a potential source of felsic igneous rock.

In conclusion, the studied saline lacustrine shales likely formed through weathering of felsic igneous and metamorphic rocks, with minor contributions from intermediate igneous rocks. Similar findings from studies conducted with sandstone samples have been reported (Fan et al., 2020; Ma et al., 2021).
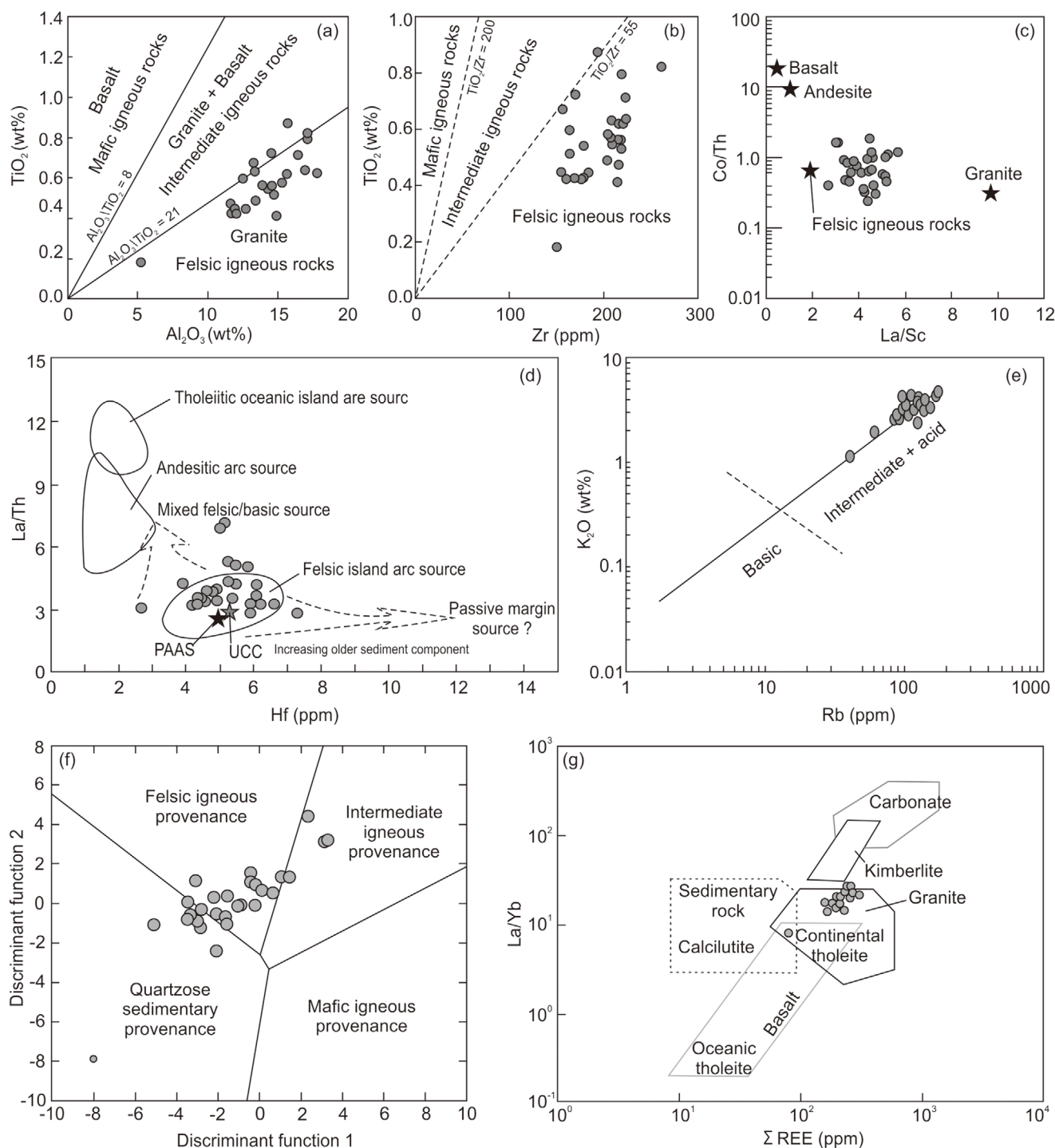
5.3. Tectonic Settings

Plate tectonic processes occurring in the sedimentary depositional basin can be reflected in the geochemistry of clastic sediments (Fathy et al., 2021). First, this study employed the Th-Sc-(Zr/10), La-Th-Sc, and Th-Co-(Zr/10) discriminatory plots, as well as the K_2O/Na_2O versus SiO_2 diagram, to better establish the sample's tectonic background (Bhatia and Crook, 1986; Roser and Korsch, 1986; Wang, W.X. et al., 2022). The studied shale samples predominantly plot in the active continental margin (ACM) field in the discrimination diagram of K_2O/Na_2O versus SiO_2 (Fig. 12a; after Roser and Korsch, 1986), while they primarily plot in or adjacent to the continental island arc (CIArc) and ACM fields in the discrimination diagrams of Sc-La-Th (Fig. 12b), Sc-Th-Zr/10 (Fig. 12c), and Zr/10-Th-Co (Fig. 12d) (after Bhatia and Crook, 1986). Three diagrams imply that the source region consisted of an ACM and a continental arc.

In addition, concentrations of the REE were also used to reflect tectonic settings (Bhatia and Crook, 1986). The La and Ce values of the Fajiaying Formation shale samples are similar to those of rocks found in a passive continental margin. Provenance rock types have RREE values and LREE/HREE ratios similar to those found in ACMs, but La/Yb and LaN/YbN ratios point to a CIArc as their tectonic setting. Input from basic and felsic materials suggests terrigenous origins near the continental shelf, where the anomaly and Ce/Ce* ratio are weakly negative.

Based on the aforementioned geochemical evidence and understanding of the correlation between CIArc and continental margins, it was concluded that the sediments used to construct the Fajiaying Formation originated primarily from an ACM and a CIArc.

5.4. Paleoweathering Condition and Climatic Change

Igneous rock decomposition results in the preferential residual Al_2O_3 enrichment in the soil profile and the removal of alkaline cations i.e., K^+, Na^+, and Ca^{2+}. Thus, the relationship between alkaline REE and alkali can be used to assess the severity of weathering in clastic sediments (Nesbitt and Young, 1982). Therefore, the weathering condition is commonly inferred from

Fig. 11. Geochemical diagrams of tectonic setting for the Fajiaying Formation samples. (a) TiO_2 vs. Al_2O_3 diagram (Hayashi et al., 1997); (b) TiO_2 vs. Zr diagram (Roser and Korsch, 1988); (c) Co/Th vs. La/Sc (Condie, 1993); (d) La/Th vs. Hf diagram (Floyd and Leveridge, 1987); (e) K_2O vs. Rb diagram (Floyd et al., 1989); (f) discriminant diagram for multi-major elements (Verma and Armstrong-Altrin, 2013); (g) La/Yb vs. ΣREE (after Roser and Korsch, 1988). The discriminant functions are: F1 = $(1.773TiO_2) + (0.0607Al_2O_3) + (0.760TFe_2O_3) + (−1.500MgO) + (0.616CaO) + (0.509Na_2O) + (−1.224K_2O) − 9.090$; F2 = $(0.445TiO_2) + (0.070Al_2O_3) + (−0.25TFe_2O_3) + (−1.142MgO) + (0.438CaO) + (1.475Na_2O) + (1.426K_2O) − 6.681$.

the terrigenous sediment's geochemical composition (e.g., Madhavaraju et al., 2017, 2019; Armstrong-Altrin et al., 2017; Absar, 2021).

Paleoweathering proxies such as (CIA = $[Al_2O_3/(Al_2O_3 + CaO^*$ $+ K_2O + Na_2O)] × 100$; Nesbitt and Young, 1982) and (CIW = $[Al_2O_3/(Al_2O_3 + Na_2O + CaO^*)] × 100$; Harnois, 1988) have been successfully used to interpret the source area's weathering condition (Fathy et al., 2021; Ramirez-Montoya et al., 2021 and references
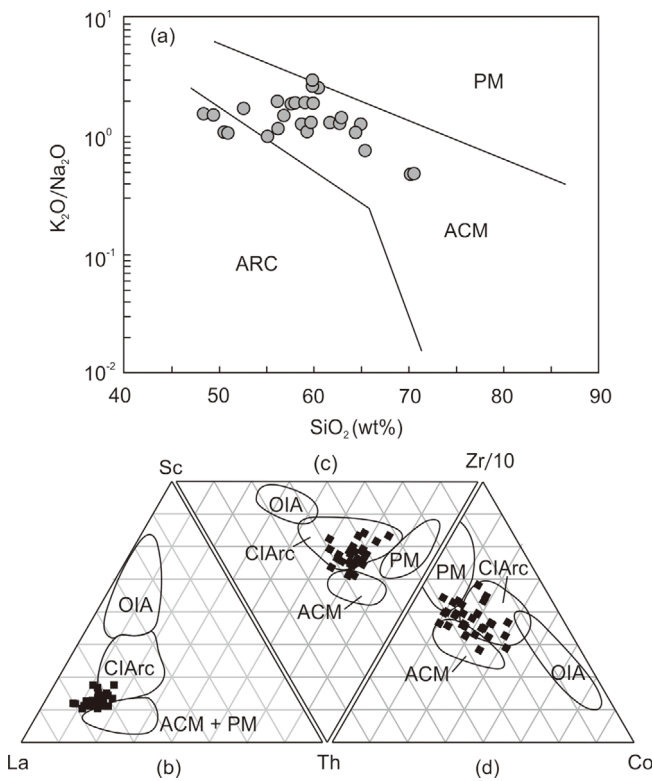
Fig. 12. (a) K$_2$O/Na$_2$O vs. SiO$_2$, (b) Sc-La-Th, (c) Th-Sc-Zr/10, and (d) Zr/10-Th-Co diagrams for the shales from the Fajiaying Formation (Bhatia and Crook 1986). Trace elements are plotted in ppm. ACM = active continental margin; CIArc = continental island arc; ARC, OIA = oceanic island arc; PM = passive margin.

therein).

Where CaO* indicates the incorporated calcium in silicate minerals and all oxides were expressed in molar concentrations (Fedo et al., 1995). According to McLennan's methodology, CaO associated with non-silicate minerals (phosphate and carbonate) was excluded (1993): (1) Using the formula CaO' = CaO − 10/3

× P$_2$O$_5$, CaO in apatite was corrected for P$_2$O$_5$ data. (2) If CaO' is greater than Na$_2$O, the final CaO* value is set to that of Na$_2$O; otherwise, it is set to CaO'.

The CIA values for Fajiaying Formation shales ranged from 40.68 to 67.16 wt%, while the CIW values range from 58.77 to 83.26 wt% (Table 1). The average CIA and CIW values revealed the exposure of studied samples to a low chemical weathering condition. Furthermore, the CIA versus ICV diagram suggests that the source weathering is relatively weak, or that there is no chemical weathering based on compositionally mature alumina-rich minerals (Fig. 13a). This result is supported by the A-CN-K ternary diagram (Fig. 8c). Furthermore, bivariate Scatter Plot of K$_2$O + Al$_2$O$_3$ + Na$_2$O and SiO$_2$ show that the source area was an arid environment (Fig. 13b). This study can thus interpret the extremely weak chemical weathering in source terrain under arid conditions, which is consistent with the greenhouse climate background in East China during the Early Cretaceous (Zhang et al., 2020a, 2021a; Wang, X.X. et al., 2022).

It should be noted that the shale sample's CIA values from different sections may differ due to the different weathering intensities in the source composition. In general, the CIA and CIW values of the studied shale samples increased from the bottom to the top of the formation, indicating the increased chemical weathering (Table 1 and Fig. 14). The association between climate change and chemical weathering conditions was evaluated using paleoclimatic proxy indexes such as Sr/Cu, Rb/Sr, and Al$_2$O$_3$/MgO. Sr/Cu values were observed to decrease gradually as formation height increased, while Rb/Sr and Al$_2$O$_3$/MgO values increased gradually (Fig. 14). Obviously, the paleoclimate shifted from dry and hot to warm and wet conditions. Thus, it is concluded that a such change in paleoclimate resulted in a gradual increase in weathering degree (Fig. 14).
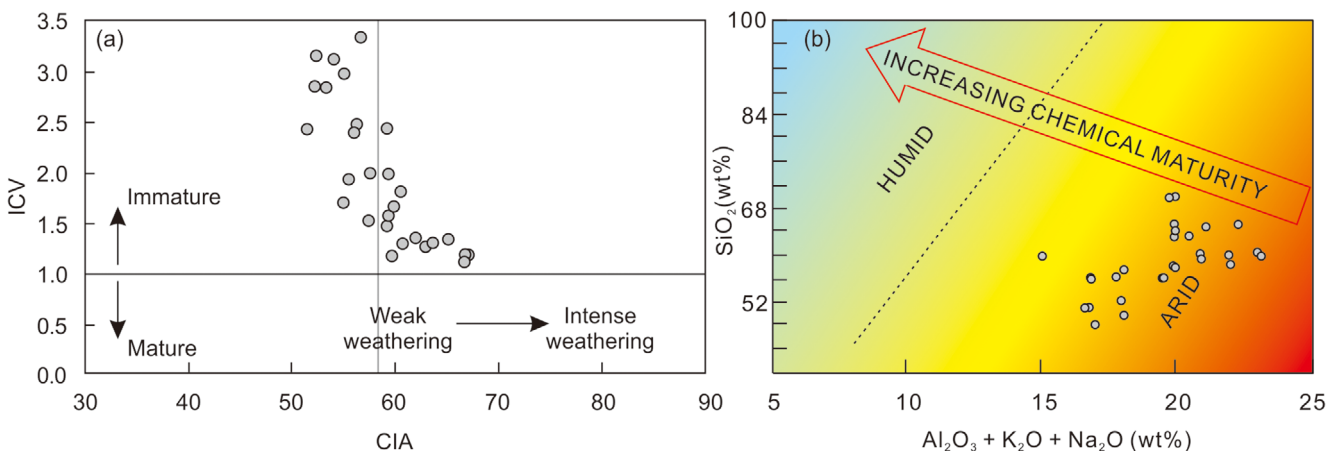
Fig. 13. (a) CIA vs. ICV diagram (after Nesbitt and Young, 1984; Cox et al., 1995). The grey field represents the average CIA value. (b) Geochemical diagrams of paleoclimate condition (Suttner and Dutta, 1986).
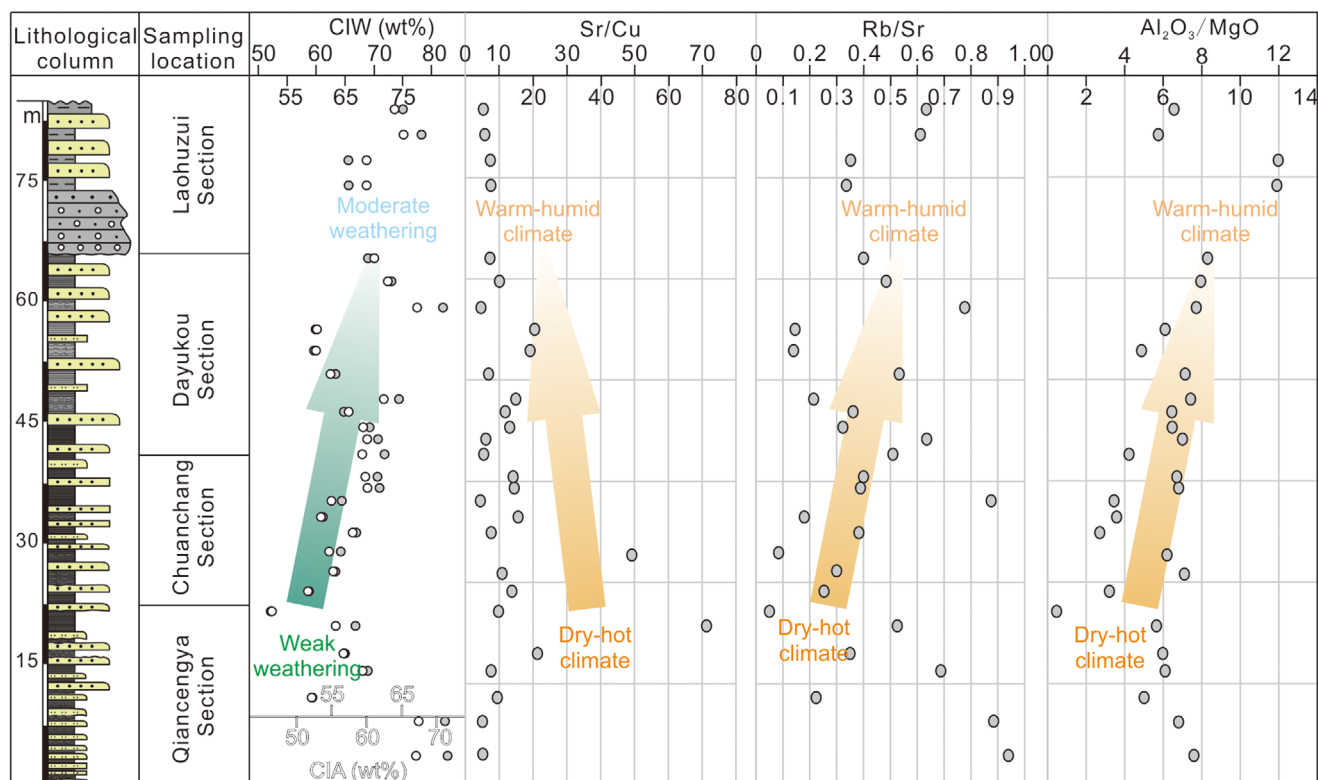
Fig. 14. Vertical variations of paleoclimatic proxy indexes and paleoweathering proxies (CIA and CIW) (modified after Wang, W.X. et al., 2022).

6. CONCLUSIONS

The geochemistry of the salt lacustrine shale deposits from the Early Cretaceous has led to the following results.

(1) There was no discernible change in sediment source from the bottom to the top of the formation in the investigated saline lacustrine shales, suggesting that they developed from the weathering of felsic igneous rocks.

(2) According to the results of several tectonic discrimination diagrams, the sediments originated from a CIArc and ACM environment.

(3) In the source terrain, the process of chemical weathering was very weak because of the arid conditions. It is essential to observe that the change from a dry, hot climate to a warm, humid climate coincided with an obvious rise in chemical weathering.

ACKNOWLEDGMENTS

REFERENCES

Absar, N., 2021, Mineralogy and geochemistry of siliciclastic Miocene Cuddalore Formation, Cauvery Basin, South India: implications for provenance and paleoclimate. Journal of Paleogeography (English Edition), 10, 602–630.

Armstrong-Altrin, J.S., Lee, Y.I., Kasper-Zubillaga, J.J., and Trejo-Ramírez, E., 2017, Mineralogy and geochemistry of sands along the Manzanillo and El Carrizal beach areas, southern Mexico: implications for paleoweathering, provenance, and tectonic setting. Geological Journal, 52, 559–82.

BGMRSD (Bureau of Geology and Mineral Resources of Shandong Province), 1991, Regional Geology of Shandong Province. Geological Publishing House, Beijing, 595 p.

Bhatia, M.R. and Crook, K.A.W., 1986, Trace element characteristics of greywackes and tectonic setting discrimination of sedimentary basin. Contributions to Mineralogy and Petrology, 92, 181–93.

Bottini, C., Cohen, A.S., Erba, E., Jenkyns, H.C., and Coe, A.L., 2012,

Osmium-isotope evidence for volcanism, weathering, and ocean mixing during the early Aptian OAE 1a. Geology, 40, 583–586.

Charbonnier, G., Adatte, T., Spangenberg, J.E., and Föllmi, K.B., 2018, The expression of early Aptian to latest Cenomanian oceanic anoxic events in the sedimentary record of the Briançonnais domain. Global and Planetary Change, 170, 76–92.

Chen, X., Sageman, B.B., Yao, H.W., Liu, S.A., Han, K.B., Zou, Y., and Wang, C.S., 2021, Zinc isotope evidence for paleoenvironmental changes during Cretaceous Oceanic Anoxic Event 2. Geology, 49, 412–416.

Condie, K.C., 1993, Chemical composition and evolution of the upper continental crust: contrasting results from surface samples and shales. Chemical Geology, 104, 1–37.

Cox, R., Lowe, D.R., and Cullers, R.L., 1995, The influence of sediment recycling and basement composition on evolution of mudrock chemistry in the southwestern United States. Geochimica et Cosmochimica Acta, 59, 2919–2940.

Cullers, R.L., 1994, The controls on the major and trace element variation of shales, siltstones, and sandstones of Pennsylvanian–Permian age from uplifted continental blocks in Colorado to platform sediment in Kansas, USA. Geochimica et Cosmochimica Acta, 58, 4955–72.

Cullers, R.L., 1995, The controls on the major- and trace-element evolution of shales, siltstones and sandstones of Ordovician to Tertiary age in the Wet Mountains region, Colorado, USA. Chemical Geology, 123, 107–131.

Cullers, R.L., DiMarco, M.J., Lowe, D.R., and Stone, J., 1993, Geochemistry of a silicified, felsic volcaniclastic suite from the early Archaean Panorama Formation, Pilbara Block, western Australia: an evaluation of depositional and post-depositional processes with special emphasis on the rare-earth elements. Precambrian Research, 60, 99–116.

Cullers, R.L. and Podkovyrov, V.N., 2000, Geochemistry of the Mesoproterozoic Lakhanda shales in southeastern Yakutia, Russia: implications for mineralogical and provenance control, and recycling. Precambrian Research, 104,77–93.

Erba, E., 1994, Nannofossils and superplumes: the Early Aptian "nannoconid crisis". Paleoceanography, 9, 483–501.

Fan, A.P., Sun, S.N., Yang, R.C., Zhang, Z., De, S., Nenzhelele, J.D.N., Li, Y., Liu, H.P., Zhou, Y.Q., and Yuan, J., 2020, Provenance analysis of the Cretaceous Laiyang Group on Lingshan Island (western Yellow Sea, China) and its tectono-sedimentary implications. Australian Journal of Earth Sciences, 6, 1–17.

Fan, D.J., Shan, X.L., Makeen, Y.M., He, W.T., Su, S.Y., Wang, Y.B., Yi, J., Hao, G.L., and Zhao, Y.T., 2021, Response of a continental fault basin to the global OAE1a during the Aptian: Hongmiaozi Basin, Northeast China. Scientific Reports, 11, 7229.

Fathy, D., Wagreich, M., Ntaflos, T., and Sami, M., 2021, Provenance characterization of Campanian lacustrine organic-rich mudstones on the southern Tethyan margin, Egypt. ACS Earth and Space Chemistry, 5, 197–209.

Fedo, C.M., Nesbitt, H.W., and Young, G.M., 1995, Unraveling the effects of potassium metasomatism in sedimentary rocks and paleosols, with implications for paleoweathering conditions and provenance. Geology, 23, 921–924.

Fernández-Mendiola, P.A., Mendicoa, J., Owen, H.G., and Garci'a-

Monde'jar, J., 2018, The Early Aptian (Cretaceous) stratigraphy of Mount Pagasarri (N Spain): oceanic anoxic Event-1a. Geological Journal, 53, 1802–1822.

Floyd, P.A. and Leveridge, B.E., 1987, Tectonic environment of the Devonian Gramscatho basin, south Cornwall: framework mode and geochemical evidence from turbiditic sandstones. Journal of the Geological Society, 144, 531–42.

Floyd, P.A., Winchester, J.A., and Park, R.G., 1989, Geochemistry and tectonic setting of Lewisian clastic metasediments from the Early Proterozoic Loch Maree Group of Gairloch, NW Scotland. Precambrian Research, 45, 203–214.

Gao, B. and Li, Z., 2018, The Early Cretaceous sedimentary-tectonic attributes of Lingshan Island Basin, East Shandong Province, China: constraints from the chemical compositions of detrital heavy minerals. Geological Journal, 55, 584–595.

Harnois, L., 1988, The CIW index: a new chemical index of weathering. Sedimentary Geology, 55, 319–322.

Hayashi, K.I., Fujisawa, H., Holland, H.D., and Ohmoto, H., 1997, Geochemistry of ca. 1.9 Ga sedimentary rocks from northeastern Labrador, Canada. Geochimica et Cosmochimica Acta, 61, 4115–37.

Heimhofer, U., Hochuli, P.A., and Burla, S., 2005, Timing of Early Cretaceous angiosperm diversification and possible links to major paleoenvironmental change. Geology, 33, 141–144.

Horikx, M., Huck, S., Adatte, T., and Heimhofer, U., 2017, Vegetation dynamics, angiosperm radiation and climatic changes in the Lusitanian Basin (Portugal) during Albian times. Paleogeography, Paleoclimatology, Paleoecology, 465, 30–41.

Huber, B.T., MacLeod, K.G., Watkins, D.K., Watkins, D.K., and Coffin, M.F., 2018, The rise and fall of the Cretaceous Hot Greenhouse climate. Global and Planetary Change, 167, 1–23.

Li, X.H, Xu, W.L., Liu, W.H., Zhou, Y., Wang, Y., Sun, Y., and Liu, L., 2013, Climatic and environmental indications of carbon and oxygen isotopes from the Lower Cretaceous calcrete and lacustrine carbonates in Southeast and Northwest China. Paleogeography, Paleoclimatology, Paleoecology, 385, 171–189.

Lü, H.B., Wang, B., and Zhang, H.C., 2011, Discovery of the Late Mesozoic slump beds in Lingshan Island, Shandong, and a pilot research on the regional tectonics. Acta Geologica Sinica, 85, 938–946. (in Chinese with English abstract)

Luan, G.Z., Li, A.L., Wang, J., Li, G., and Xie, R.J., 2010, The geological origin division of the main sea island in Qingdao area and environment analysis. Periodical of Ocean University of China, 40, 111–116. (in Chinese with English abstract)

Ma, Q., Zhou, Y., Mu, H., Zhou, T., Zhao, H., Yin, X., and Liu, Y., 2022, Geochemistry of the Laiyang Group from outcrops and Lingke-1 core on Lingshan Island, Shandong Province, Eastern China: implications for provenance, tectonic setting and paleo-environment. Geological Magazine, 159, 37–54.

Madhavaraju, J., Armstrong-Altrin, J.S., Pillai, R.B., and Pi-Puig, T., 2021, Geochemistry of sands from the Huatabampo and Altata beaches, Gulf of California, Mexico. Geological Journal, 56, 2398–2418.

Madhavaraju, J., Pacheco-Olivas, S.A., Gonzalez-Leon, C.M., Espinoza-Maldonado, I.G., Sanchez-Medrano, P.A, Villanueva-Amadoz, U., Monreal, R., Pi-Puig, T., Ramirez-Montoya, E., and Grijalva-Noriega, F.J., 2017, Clay mineralogy and geochemistry of the Lower Creta-

ceous siliciclastic rocks of the Morita Formation, Sierra San José section, Sonora, Mexico. Journal of South American Earth Sciences, 76, 397–411.

Madhavaraju, J., Saucedo-Samaniego, J.C., Löser, H., Espinoza-Maldonado, I.C., Solari, L., Monreal, R., Grijalva-Noriega, F.J., and Jaques-Ayala, C., 2019, Detrital zircon record of Mesozoic volcanic arcs in the Lower Cretaceous Mural Limestone, northwestern Mexico. Geological Journal, 54, 2621–2645.

Madhavaraju, J., Tom, M., Lee, Y.I., Balaram, V., Ramasamy, S., Carranza-Edwards, A., and Ramachandran, A., 2016, Provenance and tectonic settings of sands from Puerto Peñasco, Desemboque and Bahia Kino beaches, Gulf of California, Sonora, Mexico. Journal of South American Earth Sciences, 71, 262–275.

McLennan, S.M., 1989, Rare earth elements in sedimentary rocks: influence of provenance and sedimentary processes. In: Lipin, B.R. and McKay, G.A. (eds.), Geochemistry and Mineralogy of Rare Earth Elements. Reviews in Mineralogy and Geochemistry, Mineralogical Society of America, 21, p. 169–200. https://doi.org/10.1515/9781501509032-010

McLennan, S.M., 1993, Weathering and global denudation. The Journal of Geology, 101, 295–303.

McLennan, S.M., Hemming, S., McDaniel, D.K., and Hanson, G.N., 1993, Geochemical approaches to sedimentation, provenance, and tectonics. In: Johnsson, M.J. and Basu, A. (eds.), Processes Controlling the Composition of Clastic Sediments. Geological Society of America, Special Papers, 284, p. 21–40. https://doi.org/10.1130/SPE284-p21

Moriya, K., 2011, Development of the Cretaceous greenhouse climate and the oceanic thermal structure. Paleontological Research, 15, 77–88.

Nakagawa, Y., Legrand, J., Bôle, M., Hori, R.S., Kuroda, J., Hasegawa, H., and Ikeda, M., 2022, Terrestrial and marine organic matter evidence from a Cretaceous deep-sea chert of Japan: implications for enhanced hydrological cycle during the Aptian OAE 1a. Global and Planetary Change, 215, 103886.

Nesbitt, H.W. and Young, G.M., 1982, Early Proterozoic climates and plate motions inferred from major element chemistry of lutites. Nature, 299, 715–717.

Nesbitt, H. and Young, G., 1984, Prediction of some weathering trends of plutonic and volcanic rocks based on thermodynamic and kinetic considerations. Geochimica et Cosmochimica Acta, 48, 1523–1534.

Ramirez-Montoya, E., Madhavaraju, J., and Monreal, R., 2021, Geochemistry of the sedimentary rocks from the Antimonio and Rio Asuncion Formations, Sonora, Mexico: implications for weathering, provenance and chemostratigraphy. Journal of South American Earth Sciences, 106, 103035.

Roser, B.P. and Korsch, R.J., 1986, Determination of tectonic setting of sandstone-mudstone suites using SiO_2 content and K_2O/Na_2O ratio. Journal of Geology, 94, 635–50.

Roser, B.P. and Korsch, R.J., 1988, Provenance signatures of sandstone and mudstone suites determined using discriminant function analysis of major element data. Chemical Geology, 67, 119–39.

Suttner, L.J. and Duttta, P.K., 1986, Alluvial sandstone composition and paleoclimate; I, Framework mineralogy. Journal of Sedimentary Petrology, 56, 329–345.

Taylor, S.R. and McLennan, S.M., 1985, The Continental Crust: Its Composition and Evolution. Blackwell Scientific, Oxford, UK, 312 p.

Tejada, M.L.G., Suzuki, K., Kuroda, J., Coccioni, R., Mahoney, J.J., Ohkouchi, N., Sakamoto, T., and Tatsumi, Y., 2009, Ontong Java Plateau eruption as a trigger for the early Aptian oceanic anoxic event. Geology, 37, 855–858.

Van de Kamp, P.C. and Leake, B.E., 1985, Petrography and geochemistry of feld-Spathic and mafic sediments of the northeastern Pacific margin. Transactions of the Royal Society of Edinburgh: Earth Science, 76, 411–99.

Verma, S.P. and Armstrong-Altrin, J.S., 2013, New multi-dimensional diagrams for tectonic discrimination of siliclastic sediments and their application to Precambrian basins. Chemical Geology, 355, 117–133.

Wang, J., Chang, S.C., Lü, H.B., and Zhang, H.C., 2014, Detrital zircon U-Pb age constraints on Cretaceous sedimentary rocks of Lingshan Island and implications for tectonic evolution of Eastern Shandong, North China. Journal of Asian Earth Sciences, 96, 27–45.

Wang, W.X., Gan, Z.B., Li, S.J., and Xu, Y.M., 2022, Temporal variation in the chemical index of alteration in Early Cretaceous black shale as a proxy for paleoclimate. The Journal of Geology, 130, 393–411.

Wang, X.X., Zhang, X.Y., Wang, W.X., Li, S.J., and Qin, M., 2022, Geochemical and palynological records of rapid climatic change from the early to late Aptian: evidence from the Jiaolai Basin, eastern China. Australian Journal of Earth Sciences, 69, 876–892.

Wheeler, A., Shen, J., Moore T.A., Moroeng O.M., and Liu, J.J., 2022, Paleoecology and paleoclimate of an Early Cretaceous peat mire in East Laurasia (Hailar Basin, Inner Mongolia, China). Paleogeography, Paleoclimatology, Paleoecology, 599, 111050.

Wilson, P.A., Norris, R.D., and Cooper, M.J., 2002, Testing the Cretaceous greenhouse hypothesis using glassy foraminiferal calcite from the core of the Turonian tropics on Demerara Rise. Geology, 30, 607–610.

Wu, S.F., Li, C.Y., and Huang, J., 2023, Carbon isotope of the Early Cretaceous sediments from the West Pacific and the Sulu orogenic belt: implying the global atmospheric pCO_2 changes during the Early Aptian Oceanic Anoxic Event 1a. Deep Sea Research Part I: Oceanographic Research Papers, 193, 103954.

Xie, S.W., Wu, Y.B., Zhang, Z.M., Qin, Y.C., Liu, X.C., Wang, H., Qin, Z.W., Liu, Q., and Yang, S.H., 2012, U-Pb ages and trace elements of detrital zircons from Early Cretaceous sedimentary rocks in the Jiaolai Basin, north margin of the Sulu UHP terrane: provenances and tectonic implications. Lithos, 154, 346–360.

Yang, R.C., Fan, A.P., Han, Z.Z., and Van Loon, A.J., 2017, A marine or continental nature of the deltas in the Early Cretaceous Lingshandao Formation—evidences from trace elements. Acta Geologica Sinica, 91, 367–368.

Zhang, K., Liu, R., Ding, W.J., Li, L., and Liu, Z.J., 2022, The influence of Early Cretaceous paleoclimate warming event on sedimentary environment evolution and organic matter sources in Yin'e Basin: evidence from petrology and molecular geochemistry. International Journal of Coal Geology, 254, 103972.

Zhang, Q., Wang, Y.L., Jin, W.J., and Li, C.D., 2008, Eastern China Plateau during the Late Mesozoic: evidence, problems and implication. Geological Bulletin of China, 27,1404– 1430. (in Chinese with

English abstract)

Zhang, X.Y. and Li, S.J., 2020, A lacustrine record of the early Aptian climate change by oceanic anoxic event (OAE) 1a in the Jiaolai Basin, eastern China. Journal of Asian Earth Sciences, 203, 104537.

Zhang, X.Y., Li, S.J., Wang, X.X., Zhao, X.L., and Yin, T.T., 2021b, Expression of the early Aptian Oceanic Anoxic Event (OAE) 1a in lacustrine depositional systems of East China. Global and Planetary Change, 196, 103370.

Zhang, X.Y., Li, S.J., and Yin, T.T., 2021a, Terrestrial expression of the Cretaceous greenhouse regime and its relationship with OAE 1a: evidence from the Jiaolai Basin, eastern China. Geological Journal, 56, 525–546.

Zhang, X.Y., Li, S.J., Yan, M.M., Wang, X.X., and Geng, G., 2020b, Early Cretaceous black shale in the Fajiaying Formation (Lingshan Island, East China): terrestrial record of hothouse climate. Journal of Asian Earth Sciences, 191, 104200.

Zhang, X.Y., Li, S.J., Zhao, X.L., Geng, G., and Yan, M.M., 2020a, The sedimentary environment of Early Cretaceous rift basin in eastern China and its response to the Faraoni event. Geosciences Journal, 24, 359–377.

Zhang, X.Y., Li, S.J., Zhao, X.L., Geng, G., and Yan, M.M., 2020c, A new understanding of the sedimentary environment of the Laiyang Group in the Lower Cretaceous of Lingshan Island, Shandong Province, East China. Acta Geologica Sinica (English Edition), 94, 1325–1338.

Zhao, G.C., Sun, M., Wilde, S.A., and Li, S.Z., 2005, Late Archean to aleoproterozoic evolution of the North China Craton: key issues revisited. Precambrian Research, 136, 177–102.

Zhong, J., 2012, The Mesozoic sedimentary rocks on Lingshan Island: are they deep-water far sourced turbidites or intra-continental deltaic sediments? – a discussion with Prof. Lu Hongbo. Geological Review 58, 1180–1182. (in Chinese with English abstract)